



## OPEN ACCESS

## EDITED BY

Seema Garg,  
Amity University, India

## REVIEWED BY

Ismael Alejandro Aguayo-Villarreal,  
University of Colima, Mexico  
Shamsuddeen Haladu,  
Imam Abdulrahman Bin Faisal University,  
Saudi Arabia

## \*CORRESPONDENCE

Yared Daniel Reta,  
✉ yaredtafe19@gmail.com  
Temesgen Debelo Desissa,  
✉ temesgen.debelo@astu.edu.et

RECEIVED 14 August 2023

ACCEPTED 24 October 2023

PUBLISHED 10 November 2023

## CITATION

Daniel Reta Y and Desissa TD (2023),  
Composites of CoFe<sub>2</sub>O<sub>4</sub>/Graphene  
oxide/Kaolinite for adsorption of lead ion  
from aqueous solution.  
*Front. Mater.* 10:1277467.  
doi: 10.3389/fmats.2023.1277467

## COPYRIGHT

© 2023 Daniel Reta and Desissa. This is an open-access article distributed under the terms of the [Creative Commons Attribution License \(CC BY\)](https://creativecommons.org/licenses/by/4.0/). The use, distribution or reproduction in other forums is permitted, provided the original author(s) and the copyright owner(s) are credited and that the original publication in this journal is cited, in accordance with accepted academic practice. No use, distribution or reproduction is permitted which does not comply with these terms.

# Composites of CoFe<sub>2</sub>O<sub>4</sub>/Graphene oxide/Kaolinite for adsorption of lead ion from aqueous solution

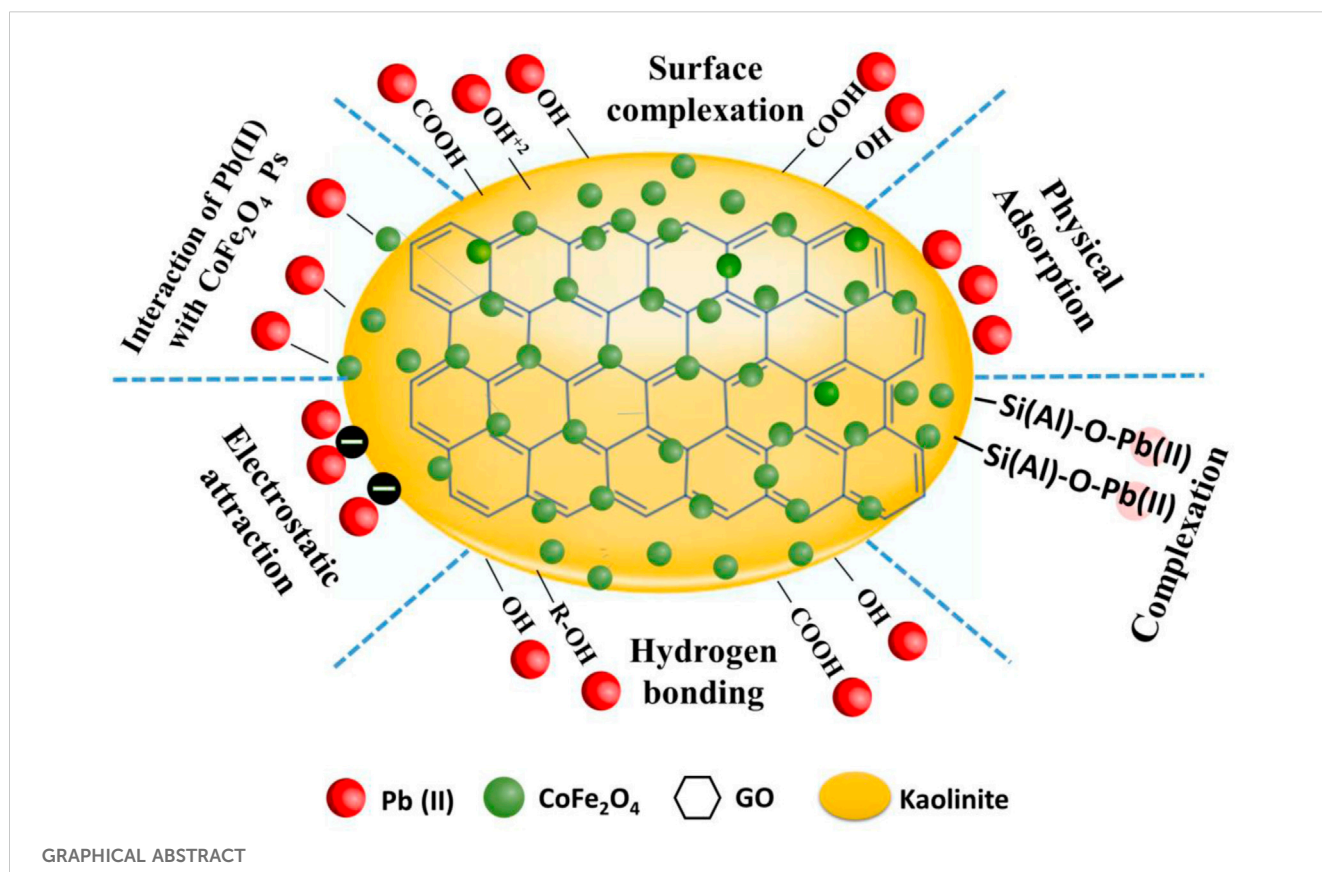
Yared Daniel Reta\* and Temesgen Debelo Desissa\*

Department of Materials Science and Engineering, Adama Science and Technology University, Adama, Ethiopia

In this work, we established composites from kaolinite (K), CoFe<sub>2</sub>O<sub>4</sub> (CF), and graphene oxide (GO) for the adsorption of the lead ion (Pb (II)). Initially, a composite of CF-GO was synthesized by hydrothermal method using cellulose bio-template extracted from false banana. The weight ratio of GO varied from 0.20 to 0.30, i.e., (1-x) CF/(x)GO (x = 0.20, 0.25, 0.30). The sample with x = 0.30, i.e., CF-0.3GO exhibited a better adsorption capacity of about 23.6 mg g<sup>-1</sup> from the binary composite samples at the initial Pb concentration of 50 mg L<sup>-1</sup>. Then, the contact time and adsorbent dosage of CF-0.3GO were optimized with the corresponding results of 90 min and 1.2 g L<sup>-1</sup>, respectively. A ternary composite was formulated from the sample of CF-0.3GO and Kaolinite (K) with the nominal composition of (1-y)K/(y)(CF-0.3GO), where y = 0.30, 0.45, 0.60, and 0.75. Among the ternary composites, the sample with a composition of 0.25K/0.75(CF0-0.3GO) showed the best adsorption capacity of about 4.2 mg g<sup>-1</sup> at the initial Pb concentration of 10 mg L<sup>-1</sup> and this sample was subsequently selected for further studies. The synthesized composites were characterized using powder X-ray diffraction (XRD), Scanning electron microscopy (SEM), Fourier transforms infrared spectroscopy (FTIR), and Differential thermogravimetric analysis (TGA-DTA), Brunauer-Emmett-Teller (BET), respectively, to determine phase purity, the particles morphology, functional groups, thermal stability, and surface area and pore volume of the of samples. Atomic absorption spectroscopy (AAS) was used to determine the adsorption capacity of samples. The effect of pH ranging from 2 to 10 was investigated for the present composite. At pH of 4, the adsorption capacity and removal efficiency changed significantly, with the corresponding results of 6.62 mg g<sup>-1</sup> and 99 %, respectively, and becomes constant. Adsorption isotherms and kinetics were investigated for a composite with a composition of 0.25K/0.75 (CF-0.3GO). The Freundlich isotherm model best fits the adsorption isotherm, with a correlation coefficient of 0.93, and the kinetic behavior followed Pseudo-second-order adsorption kinetics. Finally, the synthesized composite was stable for three-round tests toward the Pb(II) removal. Therefore, the results of this study indicate that the composites of CoFe<sub>2</sub>O<sub>4</sub>/Graphene oxide/Kaolinite could be a potential candidate for the removal of Pb (II) ions.

## KEYWORDS

CoFe<sub>2</sub>O<sub>4</sub>/Graphene oxide/Kaolinite, adsorption, lead ion, graphene oxide, kaolinite



## 1 Introduction

Water is the most essential substance for human beings' survival although its pollution by different pollutants or contaminants brings severe threats to the health of the environment and the societies (Asadi et al., 2020). These contaminants may be released from different sources into water bodies. The growth of civilization, population, and industrialization have led to a steady worsening in the purity of available water resources (Fiyadh et al., 2019).

Processing industries are the main sources of these pollutants (Obayomi and Auta, 2019), which include toxic heavy metal ions, organic dyes, particulate matter, and so on. Heavy metal ions such as Lead (Pb), Cadmium (Cd), Mercury (Hg), Tin (Sn), Iron (Fe), Manganese (Mn), Copper (Cu), Zinc (Zn), Chromium (Cr), Cobalt (Co), Arsenic (As), and Nickel (Ni) can be released from different processing industries such as mineral mining, metallurgical plating, batteries, and fertilizer plants (Yadav et al., 2019a; Es-sahbany et al., 2019). Among these different heavy and toxic metal ions Pb, Cd, Hg, and As are highly carcinogenic (Obasi and Akudinobi, 2020).

Pb (II) is an extremely toxic metal and can cause large-scale environmental pollution and health effects in many parts of the world (Monear and Xhabija, 2020). Generally, human vulnerability to lead is due to drinking water. The Environmental Protection Agency (EPA) has established zero as the ultimate pollutants level goal for lead in tap water because lead can impair human health even at low levels of exposure (Triantafyllidou and Lambrinidou, 2009).

Thus, to live in a clean environment and healthy life, the removal of Lead from water is crucial.

There are several techniques to eliminate or minimize the level of these heavy metals such as ion exchange, chemical precipitation, electrolysis, membrane separation, solvent extraction, and adsorption (Mnasri-Ghnimi and Frini-Srasra, 2019). Among these methods, adsorption is considered the most effective due to its easy operation, low cost, available adsorption materials, and high efficiency (Zheng et al., 2021).

For the adsorption process, different adsorbent materials can be utilized. The adsorbent materials include: carbon nanotubes (CNTs) (Yadav and Srivastava, 2017; Hayati et al., 2018; Fiyadh et al., 2019; Verma and Balomajumder, 2020), activated carbon (Kobya et al., 2005; Lo et al., 2012; Deliyanni et al., 2015; Nejadshafee and Islami, 2019), clay minerals with good adsorbing and ion exchangeability (Yadav et al., 2019a), porous nanomaterials (Yao et al., 2014; Lee et al., 2019) inorganic nanoparticles (Giraldo et al., 2013; Ray and Shipley, 2015; Boix et al., 2020), metal oxides (Lee, 1975; Kikuchi et al., 2006; Chen et al., 2012; Ghiloufi et al., 2016), clay-based nanocomposites (Darder et al., 2005; Das et al., 2018; Yadav et al., 2019b), and graphene oxide (Zhao et al., 2011; Tan et al., 2015; Yari et al., 2015).

Clay materials have a low cost and are most abundant so they are considered efficient adsorbent materials. For the adsorption of heavy metals most commonly used clay minerals are Kaolinite, Montmorillonite, and Bentonite (Beatrice and Olusola, 2020). To improve the adsorption performance, many researchers used modified clay minerals. For instance, a low-cost adsorbent was

produced by modifying raw kaolinite clay with concentrated sulphuric acid to remove copper and nickel from waste water (Chai et al., 2020). However, these clay minerals do not have magnetic properties that limit the reusability of clays for many cycles of operation (Wu et al., 2013). To prevent these flaws, the synthesis of composites of clay minerals with magnetic nanoparticles helps in the recovery of adsorbents (Ahmed et al., 2022; Findik, 2023). Furthermore, incorporating nanoparticles into composites enhances the surface area and pore structure of clays. (Yan et al., 2016; Olusegun and Mohallem, 2020). Spinel ferrites are commonly utilized as magnetic supports for various solid adsorbents due to their chemical and magnetic characteristics (Ahmed et al., 2022). Among magnetic spinel ferrites,  $\text{CoFe}_2\text{O}_4$  has excellent physical and chemical stability, high surface area, high saturation magnetization, high coercivity, and strong adsorption capacity (Liu et al., 2007; Mathew and Juang, 2007; Santhosh et al., 2015). However,  $\text{CoFe}_2\text{O}_4$  magnetic particles have agglomeration challenges, which can be minimized by synthesizing the  $\text{CoFe}_2\text{O}_4$  using cellulose template synthesis.

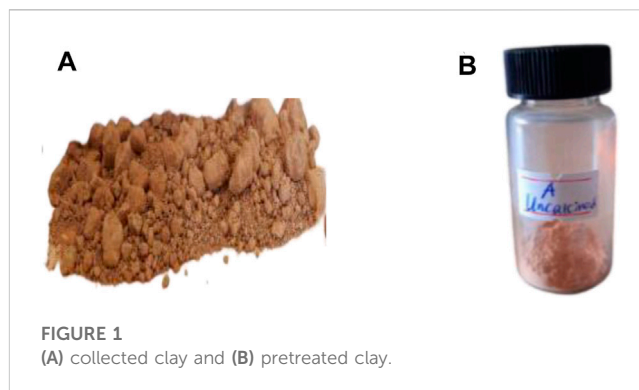
Moreover, graphene oxide (GO) may increase the surface area of clay and contain adsorption-friendly functional groups such as hydroxyl, epoxides, and carboxyl groups (Santhosh et al., 2015; Ahmed et al., 2022). As a result of these characteristics, GO appears to be a promising alternative for modifying clay minerals such as kaolinite to improve adsorption ability (Lertcumfu et al., 2020). Magnetic NPs incorporating graphene oxide have also recently been reported for heavy metal adsorption. Zhang et al., (Zhang et al., 2014), for example, reported the synthesis of magnetic  $\text{CoFe}_2\text{O}_4$ -reduced graphene oxide and its application in the removal of lead and mercury ions from aqueous solutions. Ren et al. (Ren et al., 2023) used a high-gravity reactor to manufacture a  $\text{CoFe}_2\text{O}_4$ -graphene oxide nanocomposite for Pb(II) removal and then applied it to chromium removal.

In this work, we synthesized composites from kaolinite clays and cellulose-template Cobalt ferrite ( $\text{CoFe}_2\text{O}_4$ )/Graphene oxide (GO) for adsorption of lead ions from an aqueous solution. Cellulose was extracted from the *Ensete ventricosum* (false banana). The samples were then examined using X-ray diffraction (XRD), Fourier Transform-Infrared spectroscopy (FTIR), scanning electron microscopy (SEM), thermo-gravimetric analysis-differential thermal analysis (TGA-DTA), and Brunauer-Emmett-Teller (BET). The adsorption performance of the synthesized composite materials was determined by Atomic absorption spectroscopy (AAS). The effects of contact time, adsorbent dose, and solution pH on Pb (II) adsorption were examined. Adsorption isotherm and kinetics were also investigated in order to determine the mechanism of adsorption.

## 2 Materials, chemicals, and methods

### 2.1 Materials and chemicals

Analytical grade chemicals were used for this work, including ferric nitrate nonahydrate ( $\text{Fe}(\text{NO}_3)_3 \cdot 9\text{H}_2\text{O}$ ), cobalt nitrate hydrate ( $\text{Co}(\text{NO}_3)_2 \cdot 6\text{H}_2\text{O}$ , sodium hydroxide (NaOH), graphite powder, potassium permanganate ( $\text{KMnO}_4$ ), sulfuric acid ( $\text{H}_2\text{SO}_4$ ), phosphoric acid ( $\text{H}_3\text{PO}_4$ ), hydrochloric acid (HCl),



formic acid ( $\text{CH}_2\text{O}_2$ ), acetic acid ( $\text{CH}_3\text{COOH}$ ), N, N-dimethylformamide (DMF), hydrogen peroxide ( $\text{H}_2\text{O}_2$ ), distilled water, and ethanol. The clay was collected from Wollega, Ethiopia. In addition, the false banana by-product was collected from Adama City, Ethiopia.

## 2.2 Methods

### 2.2.1 Pretreatment of clay

The collected clay (Figure 1A) was washed with distilled water ( $\text{DH}_2\text{O}$ ) and dried overnight in an oven at  $90^\circ\text{C}$ . The dried clay powder was then passed through a 75 mesh filter to create a fine powder. (Figure 1B).

### 2.2.2 Cellulose extraction

The false banana waste was cleaned to eliminate dust, dried in an oven at  $80^\circ\text{C}$ , sliced, and then extracted in three phases (Veeramachineni et al., 2016; Melikoğlu et al., 2019) as described below.

#### 2.2.2.1 Alkaline pretreatment (stage I)

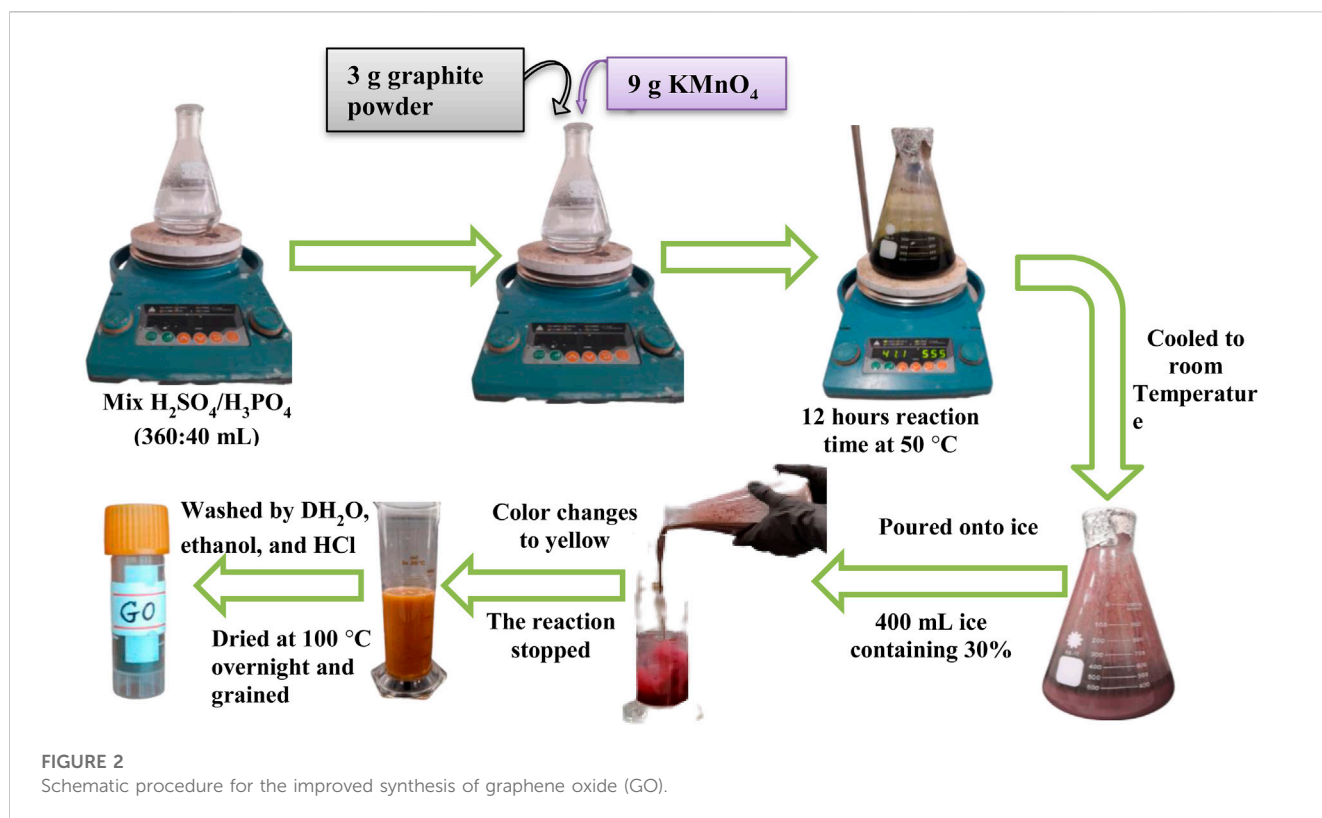
First, the false banana byproduct was boiled with 2% NaOH (1:40) w/v for 2 h to remove the remaining dust. Alkaline pretreatment was performed on a hot plate at  $90^\circ\text{C}$  for 1.5 h in 3.0 L 5% NaOH solutions with a solid to liquid ratio of dry material of 1:10 (w/v). Byproduct residues were continuously filtered and cleaned with hot distilled water.

#### 2.2.2.2 Formic acid, acetic acid, and hydrogen peroxide treatment (stage II)

The pulps were further treated with a mixture of 20% formic acid (FA)/20% acetic acid (AA)/7.5%  $\text{H}_2\text{O}_2$  (2:1:2) solution on the hotplate at  $90^\circ\text{C}$  for 1.5 h, at a byproduct to liquid ratio of 1:10. Finally, the delignified pulps were filtered to separate the cooking liquor (which contains lignin and hemicellulose) from cellulose and washed with hot water.

#### 2.2.2.3 Bleaching (stage III)

The pulps were bleached separately with 7.5%  $\text{H}_2\text{O}_2$  in alkaline media of 4% and 10% NaOH solutions at a fiber ratio of 1:10, first at room temperature for 30 min, then on a water bath at  $70^\circ\text{C}$  for 30 min. Finally, the pulps were washed repeatedly with hot distilled water to remove residual lignin and dried in an oven at  $60^\circ\text{C}$  until a constant weight was achieved.



### 2.2.3 Synthesis of graphene oxide (GO)

Figure 2 shows how graphene oxide (GO) was produced from graphite powder using an improved process with little modification (Marcano et al., 2010). The first stage includes oxidizing graphite with  $\text{KMnO}_4$  as the oxidizing agent. For this purpose, 360 mL  $\text{H}_2\text{SO}_4$  and 40 mL  $\text{H}_3\text{PO}_4$  are placed into an Erlenmeyer flask while being constantly and vigorously stirred. Then slowly about 9 g  $\text{KMnO}_4$  and 3 g graphite (3:1) were added to the  $\text{H}_2\text{SO}_4/\text{H}_3\text{PO}_4$  mixture by keeping the reaction mixture at  $50^\circ\text{C}$  for 12 h. After the oxidation step, the resulting mixture was kept overnight in a beaker containing 400 g of ice flakes and 3 mL of  $\text{H}_2\text{O}_2$  to stop the reaction of  $\text{KMnO}_4$ . The sample was centrifuged twice with deionized water (200 mL), HCl (200 mL), and ethanol (200 mL) to remove the supernatant from graphene. Finally, the compacted cake was dried in an oven at  $100^\circ\text{C}$  overnight.

### 2.2.4 Synthesis of composites

Initially, binary composites (cellulose templated CF-GO) were synthesized by altering the weight percentage of GO, after which was ternary composite synthesis using kaolinite clay and various weight ratios of  $\text{CoFe}_2\text{O}_4$ -0.3GO (CF-0.3GO).

#### 2.2.4.1 Synthesis of cellulose templated CF-GO

CF-GO composite with different graphene content (20, 25, and 30 wt %) was synthesized by the hydrothermal method with some modification (Fu and Wang, 2011). In separate beakers, a determined amount of graphene oxide powder was added to 50 mL distilled water and 0.4 g cellulose was added to 25 mL distilled water and sonicated ultrasonically for 30 min to distribute the powders uniformly. The cellulose solution was put into the GO solution, which was then stirred for 30 min to create a homogenized solution. The necessary amount of  $\text{Fe}(\text{NO}_3)_3 \cdot 9\text{H}_2\text{O}$  and  $\text{Co}(\text{NO}_3)_2 \cdot 6\text{H}_2\text{O}$  in a 2:1 ratio was added to the sonicated solution, followed

by stirring for 60 min at room temperature. After that, 2 M NaOH solution was dropped to the solution under constant stirring to adjust the pH around 10 then stirring for 10 min. The resulting mixture was placed in a 100 mL stainless autoclave lined with Teflon and heated to  $180^\circ\text{C}$  for 12 h. After allowing the reaction mixture to cool to room temperature, the precipitate was centrifuged and washed with distilled water and ethanol several times. Finally, the solution was dried in an oven at  $80^\circ\text{C}$  for 12 h and then calcined at  $400^\circ\text{C}$  for 3 h in a muffle furnace. To compare, the same method was utilized to make  $\text{CoFe}_2\text{O}_4$  without cellulose.

#### 2.2.4.2 Formulating composites from Kaolinite clay and CF-GO composite

After the synthesis of CF-GO, we formulated composite materials with kaolinite clay. First, the measured amount of kaolinite powder and different weight percent of CF-0.3GO (30, 45, 60, and 75 wt%) was dispersed by sonicating in 40 mL of N, N-Dimethylformamide in separate beakers for 30 min. The result was uniform dispersion. The CF-0.3GO solutions were then placed into a kaolinite solution, followed by another 30 min of sonication. The resulting solution was then agitated at room temperature for 3 h to generate a homogenized solution. The precipitate was then centrifuged and washed numerous times with distilled water and ethanol. Finally, the produced CF/GO/Kaolinite composite was dried for 12 h at  $80^\circ\text{C}$ .

## 2.3 Characterizations

Adsorbent phase purity was investigated using x-ray powder diffraction (XRD-700, Shimadzu, South Korea) with copper K radiation ( $\lambda_{\text{CuK}\alpha} = 1.5418 \text{ \AA}$ ), a scan speed of 4.0 deg/min, 40 kV, 30 mA, and a 2- scanning range from  $4^\circ$ – $80^\circ$ . FTIR (FT/IR-4000 series,

JASCO) was utilized to identify functional groups from a wave number of 400–4,000  $\text{cm}^{-1}$ , and TGA-DTA (DTG-60H, Shimadzu, South Korea) was used to test the thermal stability of the samples throughout a temperature range of 23°C–1000°C, and SEM (COXIEM-30, Shimadzu, South Korea) was used to determine surface morphology of the samples. BET (Quantachrome Instruments version 11.0) was used to calculate the specific surface area and porosity distribution of the samples. The samples' adsorption capacity towards Pb (II) ion was determined using an AAS (ZEE nit 700P, Atomic Flame Mode, Analytik Jena).

## 2.4 Adsorption performance measurement

For the adsorption investigation, a lead standard solution of 1,000  $\text{mg L}^{-1}$  Pb (II) in a diluted nitric acid standard for AAS (AVS TITRINORM) was utilized. Then, under typical equilibrium conditions, a series of adsorption tests were performed. To choose the best sample from the developed binary composites, 4.5 mg adsorbents were added to a 50  $\text{mg L}^{-1}$  concentration of 15 ml of Pb (II) solution in separate beakers. The samples were then sonicated for 10 min before being stirred for 150 min. Effect of contact time was studied for the binary samples by adjusting the time from 30–90 min. In addition, adsorbent dosage for the binary samples was optimized by varying doses from 0.6–2.1  $\text{g L}^{-1}$ . For the ternary composites, 22.5 mg adsorbent was utilized for a 10  $\text{mg L}^{-1}$  concentration of Pb (II) in 15 mL of solution. The effect of pH was also studied by varying the pH values from 2 to 10 by adding 0.1 M NaOH and 0.1 M  $\text{H}_2\text{SO}_4$ . Kinetic investigations were carried out by varying the period from 30–120 min. Adsorbent reusability was achieved by magnetically extracting the adsorbents from the solution and washing numerous times with distilled water. Allow the adsorbent powder to dry in an oven at 90°C for 3 h before reusing it.

## 2.5 Desorption experiment

For desorption study, 1.5  $\text{g L}^{-1}$  of produced CF/GO/Kaolinite composite was poured in 50 mL of 10  $\text{mg L}^{-1}$  Pb (II) solution at laboratory conditions of optimal initial pH, 300 rpm mixing speed, 25°C temperature, and 60 min contact time. After the adsorption test, the adsorber was separated from the aqueous phase and rinsed with distilled water several times to washout the lead ion from the adsorber surface. At the end of the intended time, the sample was then centrifuged several times with deionized water (200 mL), and ethanol (200 mL) to separate the solution and solid phase and the lead ion concentration was measured.

## 3 Results and discussions

### 3.1 Phase purity analysis

The XRD patterns of materials made of graphene oxide,  $\text{CoFe}_2\text{O}_4$ , and  $\text{CoFe}_2\text{O}_4$ -GO with different graphene content are shown in Figure 3. The diffraction pattern of graphene oxide shows a strong peak at  $2\theta = 11.3^\circ$  ( $d$ -spacing of 7.76 Å) corresponds to the (001) plane which confirms the success in the GO synthesis

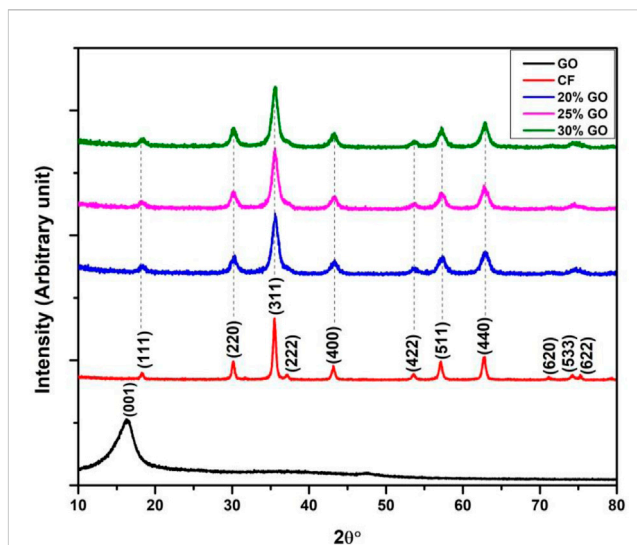


FIGURE 3 XRD pattern of, from bottom to top, graphene oxide (GO),  $\text{CoFe}_2\text{O}_4$  (CF), CF-0.2GO, CF-0.25GO, and CF-0.3GO.

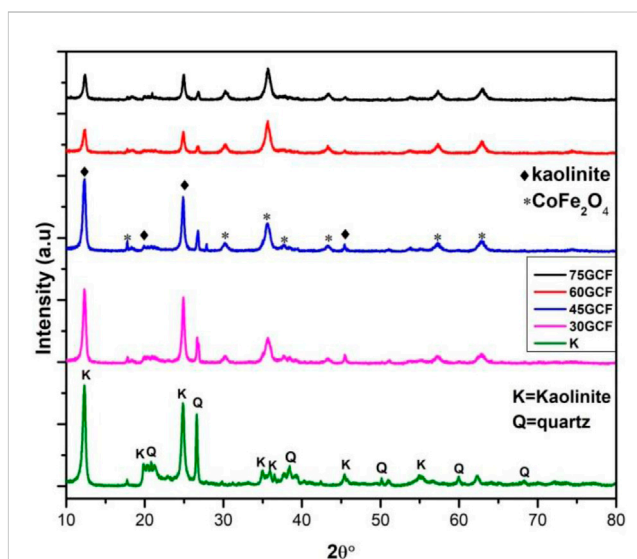


FIGURE 4 XRD Pattern of, pure kaolinite and different composition of CF-0.3GO (GCF) in the kaolinite.

(Tul Ain et al., 2019). It can be seen that the diffraction peaks of almost all  $\text{CoFe}_2\text{O}_4$  with different graphene content can be traced back to spinel-like  $\text{CoFe}_2\text{O}_4$  (JCPDS 022-1086). The diffraction peaks at  $2\theta$  values of 18.3, 30.0, 35.4, 43.1, 53.5, 56.3, and 62.4, 71.1, 74.0, and 75.2 can be assigned to the crystal planes (111), (220), (311), (400), (422), (511), (440), (622), (533), and (620) of spinel  $\text{CoFe}_2\text{O}_4$ , respectively (Zong et al., 2014; Zawrah, 2018). GO (001) pattern is not observed in CF-GO. This can be explained by the reduction of GO to graphene during the hydrothermal and calcination process (Fu and Wang, 2011).

Moreover, the reduced GO layer may decorated the  $\text{CoFe}_2\text{O}_4$  nanocrystals, resulting in the disappearance of the diffraction peak

of graphene of the (001) crystallographic plane. The XRD pattern, illustrated in Figure 4, was used to estimate the phase composition of the prepared clay. The  $2\theta$  diffraction pattern has a range of 10–80. JCPD files 058-2004 and 046-1045 indicate the existence of high-intensity diffraction peaks at  $2\theta$  of 12.39°, 19.85°, 24.96°, and 26.55°, the corresponding crystal orientation are (001), (020), (002), and (101), respectively (Zen et al., 2018; Mustapha et al., 2019). The JCPD document confirms that the main peaks of pretreated clay are kaolinite and quartz, which are usually found in kaolin as one of the main components.

It is found that kaolinite ( $\text{Al}_2\text{Si}_2\text{O}_5(\text{OH})_4$ ) has a very strong peak; there is also a sharp quartz peak. Characteristic peaks in the X-ray diffraction pattern of kaolinite/( $\text{CoFe}_2\text{O}_4$ -0.3GO) samples with different weight fractions of  $\text{CoFe}_2\text{O}_4$ -0.3GO (30%, 45%, 60%, and 75%) is also shown in Figure 4. With an increase of GCF weight fraction, (001) peak intensity of kaolinite decreased, which indicates that a composite is effectively formed between kaolinite and ( $\text{CoFe}_2\text{O}_4$ -0.3GO). Like kaolinite powder, the ternary composites has sharp and significant peaks at  $2\theta$  of 12.39°, 19.85°, 24.96°, and 26.55° with the corresponding indices of (001), (020), (002), and (101), respectively. This indicates a high existence of kaolinite in these compounds (JCPDS. No. 058-2004) (Olusegun and Mohallem, 2020). The diffraction peaks of  $\text{CoFe}_2\text{O}_4$  are also located at  $2\theta$  of 17.8°, 30.5°, 35.5°, 43.2°, 57.1°, and 62.7° with corresponding (111), (220), (311), (400), (511), and (400) crystallographic planes, respectively, according to JCPDS No. 022-1086 crystallization level. As a result, the XRD patterns demonstrate that binary and ternary composites were successfully formed.

### 3.2 Morphological analysis

Figures 5A–E shows the surface morphology of kaolinite (K), graphene oxide (GO), CF-0.3GO (without cellulose), CF-0.3GO (with cellulose) and 0.25K/0.75[(CF-0.30GO)], respectively. Figure 5 shows several layers of kaolin in which the kaolin particles are distributed with fewer aggregations. These results also showed some porous structure of the kaolinite lattice. As shown in Figure 5B layers of GO sheets were well exfoliated. The  $\text{CoFe}_2\text{O}_4$ /GO particles without cellulose template synthesis (Figure 5C) showed high agglomeration and larger particle size due to the magnetic property of  $\text{CoFe}_2\text{O}_4$ . In contrast, the  $\text{CoFe}_2\text{O}_4$ /GO composite with cellulose template synthesis showed a smaller particle size with porous morphology. This is happening because cellulose is a biopolymer with long chains and protects the formation of high agglomeration during synthesis as exhibited in Figure 5D. In addition, the porous structure is also exhibited in this morphology. Although the particles were homogenous they were aggregated at some point as seen in the SEM image. Unlike the kaolinite clay, Figure 5E depicts the homogeneous distribution of smaller particles, which may imply that the CF-0.3GO was spread uniformly across the surface of the kaolinite clay and modified the kaolinite structure.

### 3.3 FTIR analysis

The existence of functional groups was determined by examining the FTIR spectra of the GO, CF-GO, K, and K/(CF-GO). The large peak at 3416  $\text{cm}^{-1}$  for GO (Figure 6A) corresponds

to OH stretching vibration. In addition, the five peaks at 1726, 1584, 1403, 1221, 1048  $\text{cm}^{-1}$  belong to C=O stretching, aromatic C–C, C–O carboxyl, epoxy C–O and alkoxy (Li et al., 2015; Wang et al., 2019). For CF-GO, the stretching vibration O–H indicates that the peak is narrower than that of GO, and the peaks of oxygenates are quite attenuated or completely attenuated, indicating that the GO content in the CF-GO compound may be reduced (Fu and Wang, 2011), and the adsorption peak near 1622  $\text{cm}^{-1}$  can be traced back to the stretching vibration of the non-oxidized carbon.

The result of 616  $\text{cm}^{-1}$  showed that CF/GO corresponds to the valence vibrational bond of Co–O and Fe–O (metal-oxygen bond). The FTIR spectrum of the kaolinite was shown in Figure 6B. It exhibits absorption bands at 3691 and 3620  $\text{cm}^{-1}$  caused by the OH stretching vibration, and absorption bands at 1630  $\text{cm}^{-1}$ , 1035  $\text{cm}^{-1}$ , 1105  $\text{cm}^{-1}$ , and 916  $\text{cm}^{-1}$  caused by an H–O–H interlayer, a tetrahedral sheet of Si–O–Si group, Si–O stretching vibration, and Al–OH, respectively. (Mustapha et al., 2019). The peaks at 750 and 467  $\text{cm}^{-1}$  correspond to quartz, while the bands at 430  $\text{cm}^{-1}$  in kaolinite correspond to the tensile modes of Si–O, Al–O, and Si–O–Si bonds. This information provides a functional interface group involved in the adsorption process of kaolinite. The CF/GO/K peak at 1622  $\text{cm}^{-1}$  is significantly reduced, indicating that there is a strong interfacial interaction between GO, CF, and K, which improves the mechanical strength of the composite (Huang et al., 2020). After the kaolinite was corrected with GO and  $\text{CoFe}_2\text{O}_4$ , the peak area and intensity of the obtained composite material changed significantly, which may depend on the interaction between the functional groups in GO and the kaolinite structure (Foroutan et al., 2020a).

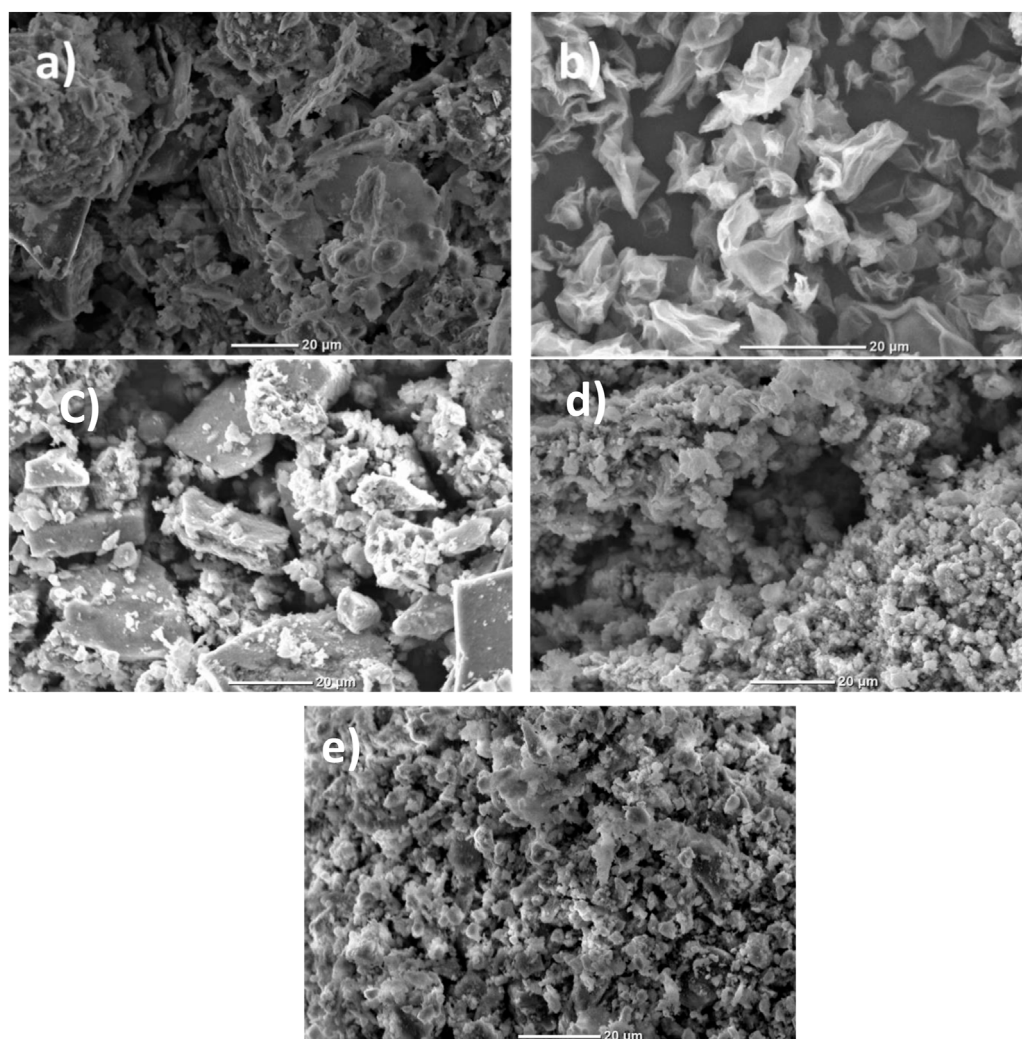
### 3.4 BET surface area and pore size analysis

Figure 7 summarizes the Brunauer-Emmett-Teller (BET) surface area and total pore volume of pretreated kaolinite, optimal binary, and ternary composite samples. The specific surface area of binary composite CF-0.3GO was 266.20  $\text{m}^2/\text{g}$ , while the ternary composite 0.25K/0.75[(CF-0.30GO)] was 577.11  $\text{m}^2/\text{g}$ . In addition, the pretreated kaolinite sample had a surface area of 519.52  $\text{m}^2/\text{g}$ . The total pore volume of CF-0.3GO and 0.25K/0.75[(CF-0.30GO)] samples was 0.089  $\text{cm}^3/\text{g}$  and 0.214  $\text{cm}^3/\text{g}$ , respectively, whereas kaolinite clay pore volume was 0.15  $\text{cm}^3/\text{g}$ .

The results indicate that the surface area and total pore volume values of ternary composites are relatively high when compared to pure kaolinite structures. The homogeneous dispersion of CF-0.3GO particles on Kaolinite creates a new surface, which contributes to the composite's increased specific surface area (Foroutan et al., 2020a). The theoretical specific surface area of graphene is known to be as high as 2630  $\text{m}^2/\text{g}$  (Fang et al., 2019). However, because of the more significant weight contribution from magnetic cobalt ferrite particles on the surface of graphene sheets, the specific surface area of the CF-0.3GO is substantially lower than the theoretical value (Ji et al., 2012).

### 3.5 Thermal property analysis

Figures 8A–C exhibit thermal analysis of kaolinite,  $\text{CoFe}_2\text{O}_4$ , and K/CF-GO composite sample from room temperature up to 800°C. The TGA and associated DTA curves reveal that all samples have different



**FIGURE 5**

The surface morphology of (A) kaolinite (K), (B) graphene oxide (GO), (C) CF-GO (without cellulose), (D) CF-0.3GO (with cellulose) and (E) K/CF-GO.

weight loss stages. The initial stage of weight loss for kaolinite,  $\text{CoFe}_2\text{O}_4$ , and K/(CF-GO) is around 3.29%, 2.55%, and 1.88%, respectively, and corresponds to the evaporation of water molecules from the surface into a crystalline structure (Romero-Guerrero et al., 2018). The second weight loss is caused by coordinated water molecules dehydrating (dehydroxylation) and clay decomposition. This is due to the degradation of organic components contained in the sample material, specifically Kaolinite and K/(CF-GO). The second weight loss of CF could be attributed to decarburization of cobalt ferrite particles (Sumathi and Kirankumar, 2016). The overall weight loss of CF was about 4.1 % and the thermal stability of CF can reach up to 800°C.

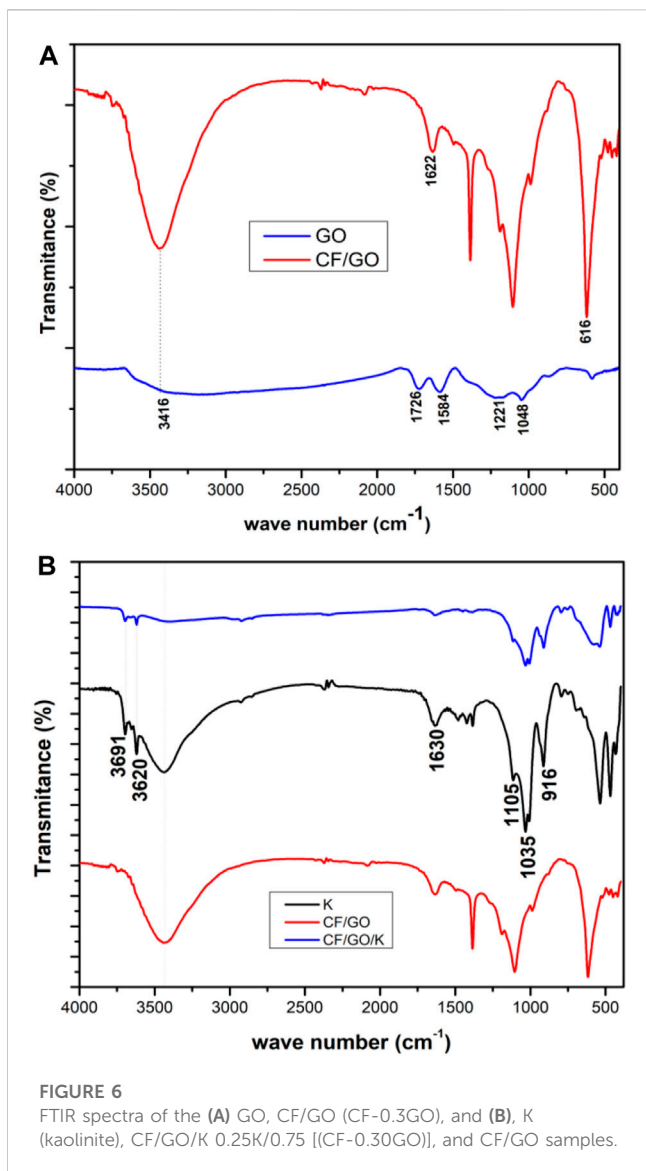
The onset temperature ( $T_{\text{onset}}$ ) at the second stage of weight loss is around 426°C, 150°C, and 400°C for K, CF, and K/CF-GO samples, respectively. For the same stage of weight loss, the equivalent ending temperature ( $T_{\text{finish}}$ ) is approximately 616°C, 500°C, and 700°C for K, CF, and K/CF-GO samples, respectively. The overall weight loss of Kaolinite was around 13.67%, whereas the K/CF-GO was approximately 6.31%. This suggests that the introduction of stable CF particles into the kaolinite improves the thermal stability of K/CF-GO.

### 3.6 Magnetic property of $\text{CoFe}_2\text{O}_4$ -Graphene/Kaolinite adsorbents

The magnetic properties of  $\text{CoFe}_2\text{O}_4$  enhance the separation for the prepared composites. We studied the magnetic separation properties of the  $\text{CoFe}_2\text{O}_4$ -Graphene/Kaolinite adsorbents. As demonstrated in Figure 9, the catalyst with homogeneous dispersion is highly responsive to an external magnetic field and can be easily isolated from the reaction mixture using a permanent magnet in less than 1 min.

### 3.7 Adsorption performance analysis

To determine the adsorption behavior of the composite, a series adsorption test was carried out with compositions  $(1-x)\text{CF}/(x)\text{GO}$  ( $x = 0.20, 0.25, 0.30$ , weight percentage of GO). The removal efficiency/adsorption (%) and adsorption capacity of the materials can be estimated using Eqs 1, 2, as shown below (Alshameri et al., 2019).



$$\text{Adsorption (\%)} = \frac{C_i - C_f}{C_i} \times 100 \quad (1)$$

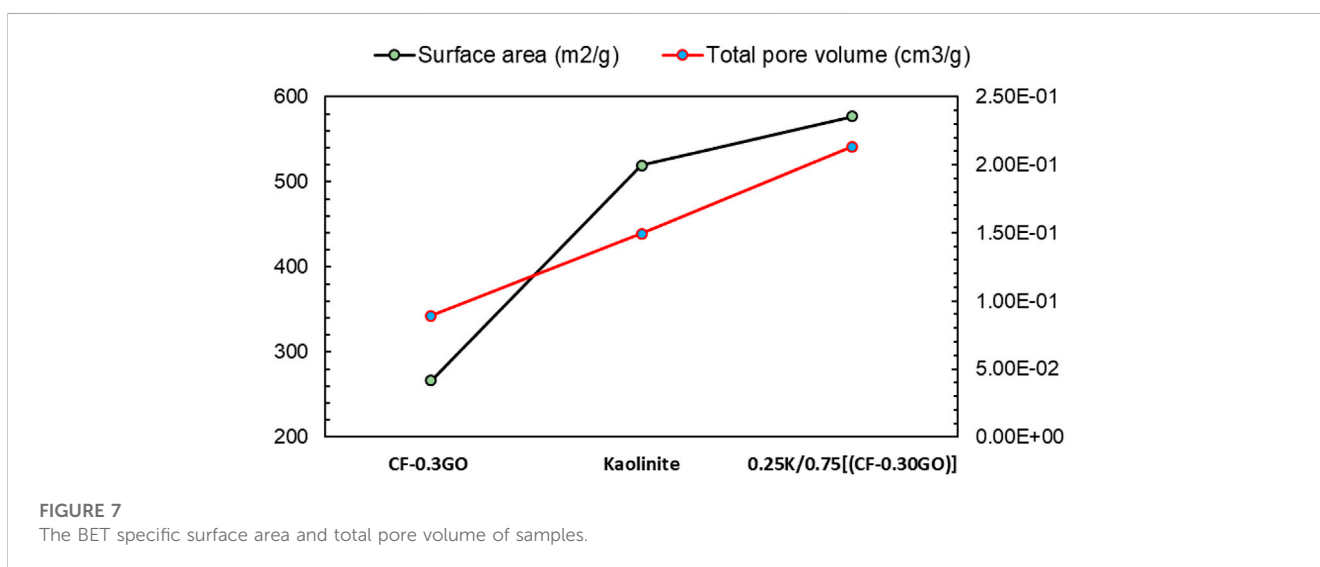
$$q_e \text{ (mg g}^{-1}\text{)} = \frac{V(C_i - C_e)}{M} \quad (2)$$

where  $C_i$  and  $C_f$  are the initial and final metal ion concentration;  $q_e$  and  $C_e$  are equilibrium adsorption capacity and concentration of the metal ions at equilibrium;  $V$  is the volume of solution (L) and  $M$  is the mass of adsorbent in grams. Figure 10 depicts the adsorption capability of (1-x)CF/(x)GO with  $x = 0.20, 0.25,$  and  $0.30$  weight ratios of GO. The sample with  $x = 0.3$ , i.e., CF-0.3GO, showed the maximum adsorption capacity of roughly  $23.6 \text{ mg g}^{-1}$  among the produced binary composites. As a result, this sample was chosen for future research and given the named GCF.

As shown in Figure 10, the adsorption capacity of Pb (II) using CF-GO increased as the amount of GO increased. Moreover, graphene oxide has a large surface area and contains many functional oxygen groups, such as hydroxyl and carboxyl groups (Chen et al., 2017; Lertcumfu et al., 2020). Therefore, with the increase of GO, the increase in the adsorption capacity of Pb (II) can be explained by the increase in surface area and surface-active sites of the adsorbent (Wang et al., 2017; He et al., 2018). This result indicates that the addition of graphene oxide improves the adsorption performance of  $\text{CoF}_2\text{O}_4$  on Pb (II).

### 3.7.1 Effect of contact time and adsorbent dosage on GCF

The effect of contact time on the decrease of Pb (II) content in GCF is shown in Figure 11A. Pb adsorption is carried out in GCF,  $C_i = 10 \text{ mg L}^{-1}$  and adsorbent dose =  $60 \text{ mg L}^{-1}$  to optimize the contact time between ions and adsorbent at room temperature. Initially, the adsorption rate of Pb (II) increases rapidly with time and then reaches equilibrium. The adsorption occurs quickly, due to the presence of active and vacant sites on the surface of the adsorbent in the initial stage (Foroutan et al., 2020a). Figure 11A clearly illustrates that the optimal period for Pb removal is 90 min. At this point, the adsorption rate equals the desorption rate, and as time passes, the active site becomes inaccessible, resulting in a decrease in



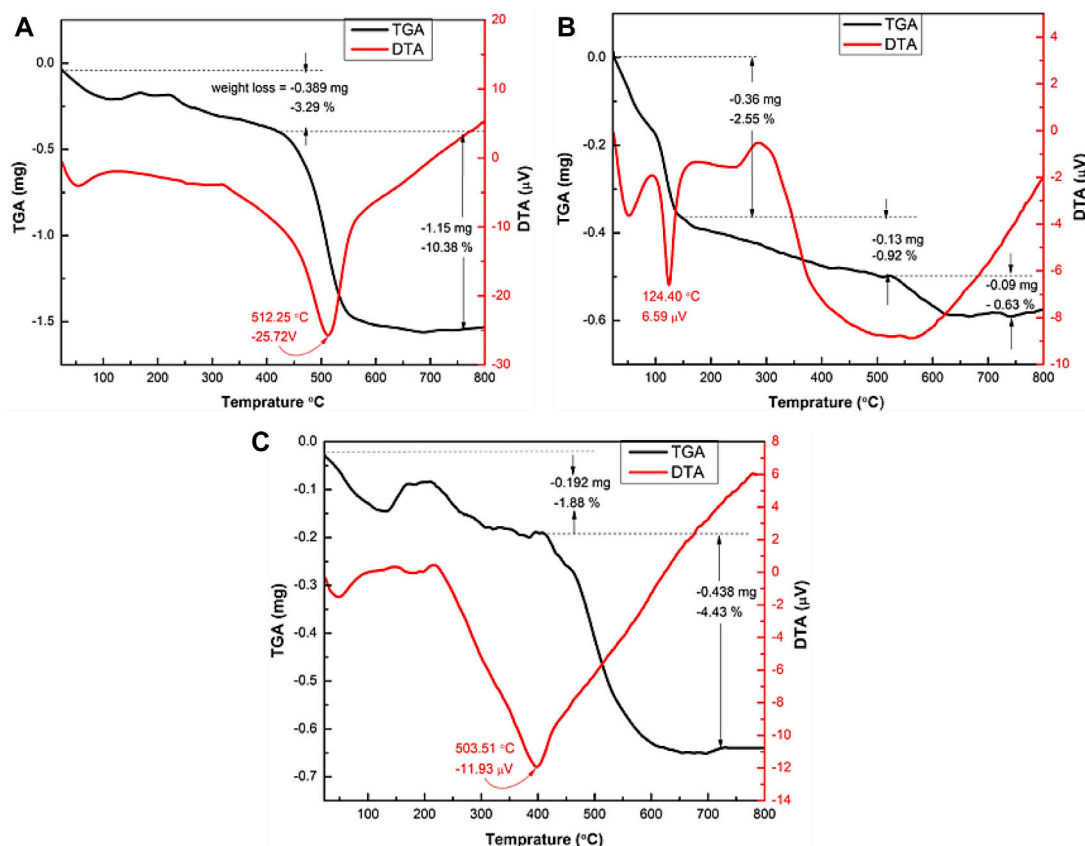


FIGURE 8 TGA-DTA analysis of (A) kaolinite (K), (B) CoFe<sub>2</sub>O<sub>4</sub> (CF), and (C) K/CF-GO 0.25K/0.75[(CF-0.30GO)].

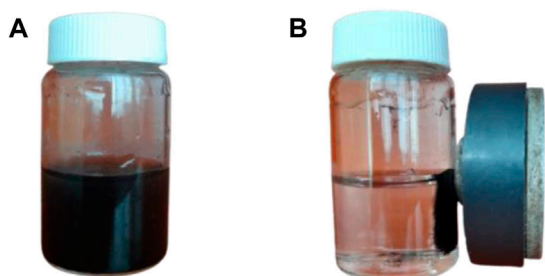


FIGURE 9 Images of 0.75[(CF-0.30GO)/0.25K] suspension without (A) and with (B) a magnetic field.

driving force and a decline in the adsorption rate (Santhosh et al., 2015). However, increasing the contact time results in a decrease in the amount of Pb. This brief effect could be attributed to metal ion saturation of the adsorbent surface, followed by the adsorption and desorption processes (Mustapha et al., 2019). As a result, 90 min is thought to be the optimal time to maximize GCF adsorbent dose. The effect of GCF adsorbent dosage on Pb ion removal was investigated by increasing the dose from 0.6 to 2.1 g L<sup>-1</sup>, as shown in Figure 11B.

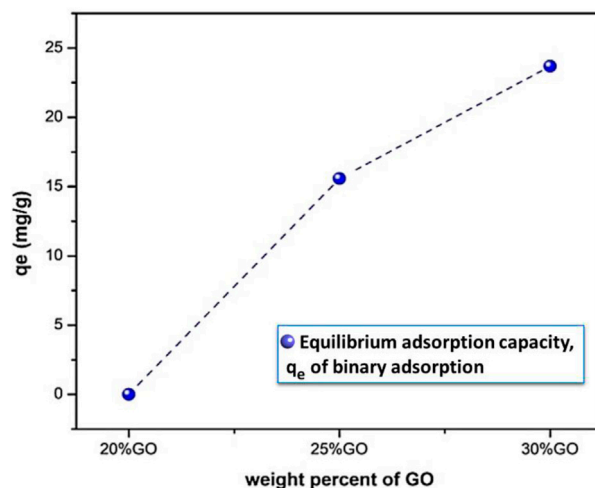


FIGURE 10 The equilibrium adsorption capacity of CF-GO composites with different GO loading initial concentrations of 50 mg L<sup>-1</sup>, at a temperature of 25°C.

The elimination effectiveness of Pb ions was raised with a rise of adsorbent dose, which can be associated with the existence of a lot of active sites on the surface of adsorbent for adsorption

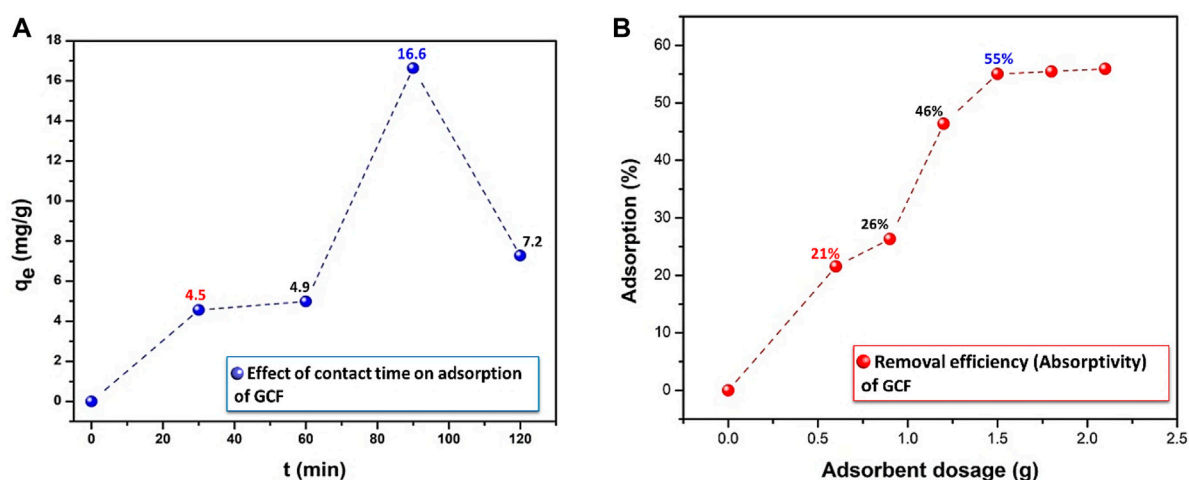


FIGURE 11

Effect of (A) contact time and (B) adsorbent dosage on the percentage of lead ion on to GCF, initial concentration of  $10 \text{ mg L}^{-1}$ ,  $T = 25^\circ\text{C}$ .

(Foroutan et al., 2019). Because all of the active sites may not be readily available for adsorption, saturation will result. The saturation factor for Pb(II) ions was  $1.5 \text{ g L}^{-1}$  for GCF, with a removal efficiency of 55%. As a result,  $1.5 \text{ g L}^{-1}$  adsorbent was taken as the optimal adsorbent dosage values for more detailed examinations. After optimizing the contact time and the dose of the binary compound (GCF), the ternary composites, i.e.,  $(y)[(\text{CF}-0.30\text{GO})]/(1-y)\text{K}$ , where  $y = 0.3, 0.45, 0.60,$  and  $0.75$ , were synthesized. The adsorption capacity was then assessed. The adsorption capacity of the produced ternary composites is shown in Figure 12. Among other composite materials, a sample with the composition  $0.25\text{K}/0.75[(\text{CF}-0.30\text{GO})]$  had the highest adsorption capacity, around  $4.2 \text{ mg g}^{-1}$ . This sample is then employed in further experiments, such as pH fluctuations, contact time, adsorption isotherm and kinetics.

### 3.7.2 Effect of pH and contact time for the ternary composite

The effect of pH on the adsorption performance of  $0.25\text{K}/0.75[(\text{CF}-0.30\text{GO})]$  was investigated, as shown in Figure 13A, because this has a direct effect on the adsorption performance. Both metal ions have an initial concentration of  $10 \text{ mg L}^{-1}$  at  $25^\circ\text{C}$ .

The pH range of Pb ions with the same metal ion concentration is 2–10. Figure 13A shows that the adsorption increases with the increase of pH under acidic conditions (2–4) significantly, and then reaches a peak at pH 4 and then all points are flattened. At pH 4, the adsorption capacity and removal efficiency become  $6.6 \text{ mg g}^{-1}$  and 99%, respectively.

At low pH ( $\text{pH} = 2$ ), the removal ability of the Pb ion was 63.5%, which may be due to the high concentration of  $\text{H}^+$  ion in the medium, so the ion occupies the active sites (Elass et al., 2011). The initial pH value increases, the amount of  $\text{H}^+$  in the medium decreases, and the competition between  $\text{H}^+$  and metal ions on the adsorber surface might be reduced, which significantly improves the efficiency of the adsorption method (Naem et al., 2019).

The percentage of Pb (II) adsorbed onto the present composite was also examined as a function of contact time (Figure 13B). First,

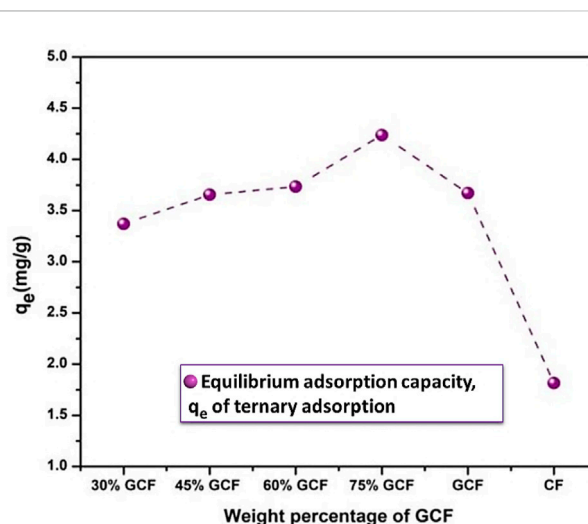


FIGURE 12

Adsorption capacity ( $q_e$ ) of  $\text{CoFe}_2\text{O}_4$  (CF), CF-0.3-GO (GCF), and K/GCF composites with different GCF loading on kaolinite, initial concentration of  $10 \text{ mg L}^{-1}$ ,  $T = 25^\circ\text{C}$ .

the adsorption rate of Pb (II) increases rapidly with time and the adsorption capacity becomes higher after 30 min. Then there is an almost small increase in adsorption rates. Compared with the adsorption from 30 min to 120 min, the adsorption capacity after 90 min was  $6.64 \text{ mg g}^{-1}$ , as a result, the 90 min time was chosen as the equilibrium time for the isotherm and kinetics study.

### 3.8 Adsorption isotherm analysis

The Freundlich, Langmuir, and Temkin isotherm models were used to assess the adsorption capacity of the ternary composite material,  $0.25\text{K}/0.75[(\text{CF}-0.30\text{GO})]$ . The Freundlich isotherm is a nonlinear sorption model that assumes a monolayer adsorption

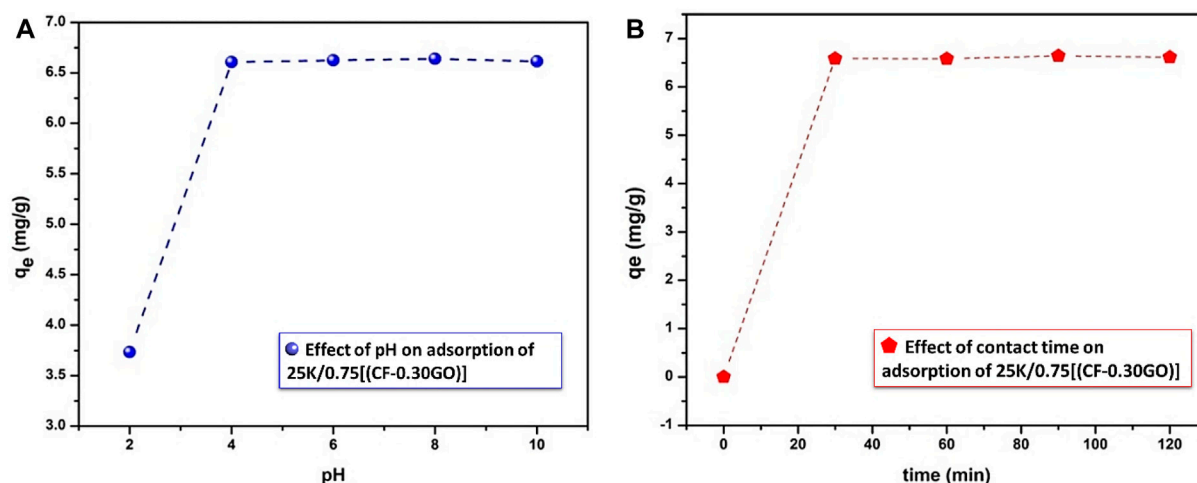


FIGURE 13 Effect of (A) pH (B) contact time on percentage of lead adsorption onto 0.25K/0.75[(CF-0.30GO)] composite material, initial conc. 10 mg/L, T = 25°C.

process on heterogeneous surfaces and provides no over-loading even at high concentrations (Lindholm, 2004). This procedure also involves interaction between the adsorbed species (Bany-Aiesh et al., 2015). The equation for this model is given in equation (3) below.

$$q_e = K_F C_e^{1/n} \quad (3)$$

Where:

1/n = an adsorption intensity on adsorbing surfaces that varies with the heterogeneity of the adsorbed monolayer.

$K_F$  = Freundlich constant, which quantifies sorption capacity.

Both of n and  $K_F$  are related to the strength of the adsorbent-adsorbent contact and the distribution of bond strength among the surface locations of heterogeneous sorbents. Figure 14A, which is a nonlinear plot produced by plotting  $q_e$  versus  $C_e$ , can be used to calculate the values of  $K_F$  and n, which are stated in Table 1. The non-linear version of the Freundlich isotherm appears to offer an adequate and relevant model of the adsorption process based on the  $R^2$  value (0.93).

The Langmuir isotherm model is a non-linear theoretical explanation of the adsorption process that suggests that adsorption occurs on homogeneous surfaces with no interaction between deposited Pb (II) (Alatalo et al., 2013). Its expression is given by Eq. 4 below.

$$q_e = \frac{q_{max} b C_e}{1 + b C_e} \quad (4)$$

Where:

b ( $1\text{mg}^{-1}$ ) = Absorption ability corresponds to the Langmuir adsorption constant.

$q_{max}$  = The adsorbent's maximal adsorption capability ( $\text{mg g}^{-1}$ ) for a full monolayer.

Figure 14B and Table 1 illustrate some values derived from a non-linear plot of  $q_e$  against  $C_e$  using Eq. 4. The plot of  $q_e$  versus  $C_e$  (14b) was found to be non-linear, with an  $R^2$  value of (0.24), indicating that the Langmuir model was not acceptable for predicting the adsorption isotherm of lead ions.

Temkin Isotherm features a component that explicitly examines interactions between adsorbing species and adsorbate (Temkin and Pyzhev, 1940; Bany-Aiesh et al., 2015). This isotherm assumes that adsorption has a uniform distribution of binding energies up to maximum binding energy and that the heat of adsorption of all molecules in the layer decreases linearly with coverage due to adsorbate-adsorbent interactions. The equation explaining the Temkin isotherm model is provided below in Eq. 5:

$$q_e = \frac{RT}{b} \ln (K_T C_e) \quad (5)$$

Where:

$K_T$  = The equilibrium binding constant of the Temkin isotherm (L/g)

R = universal gas constant (8.314 J/mol/K)

T = Temperature at 298 K.

$$B1 = \frac{RT}{b} \quad (6)$$

Based on the non-linear Temkin isotherm, as illustrated in Figure 14C. According to the correlation coefficient ( $R^2 = 0.78$ ), the composite adsorption moderately followed the Temkin model as well. The non-linear isotherm constants and coefficients of the Temkin isotherm model are also shown in Table 1. In summary, the  $R^2$  value for the Freundlich adsorption isotherms is closer to 1 than for the Langmuir and Temkin adsorption isotherms, indicating that multilayer adsorption occurs in this system.

### 3.9 Adsorption Kinetics

A kinetic model suited for data analysis, mass transfer, and chemical reactions is required to investigate the mechanism of controlling adsorption. The adsorption data in this study conforms to two kinetic models: Lagergren pseudo-first-order and pseudo-second-order. The kinetic models were studied using the derived data in Table 2. The first-order kinetic model is

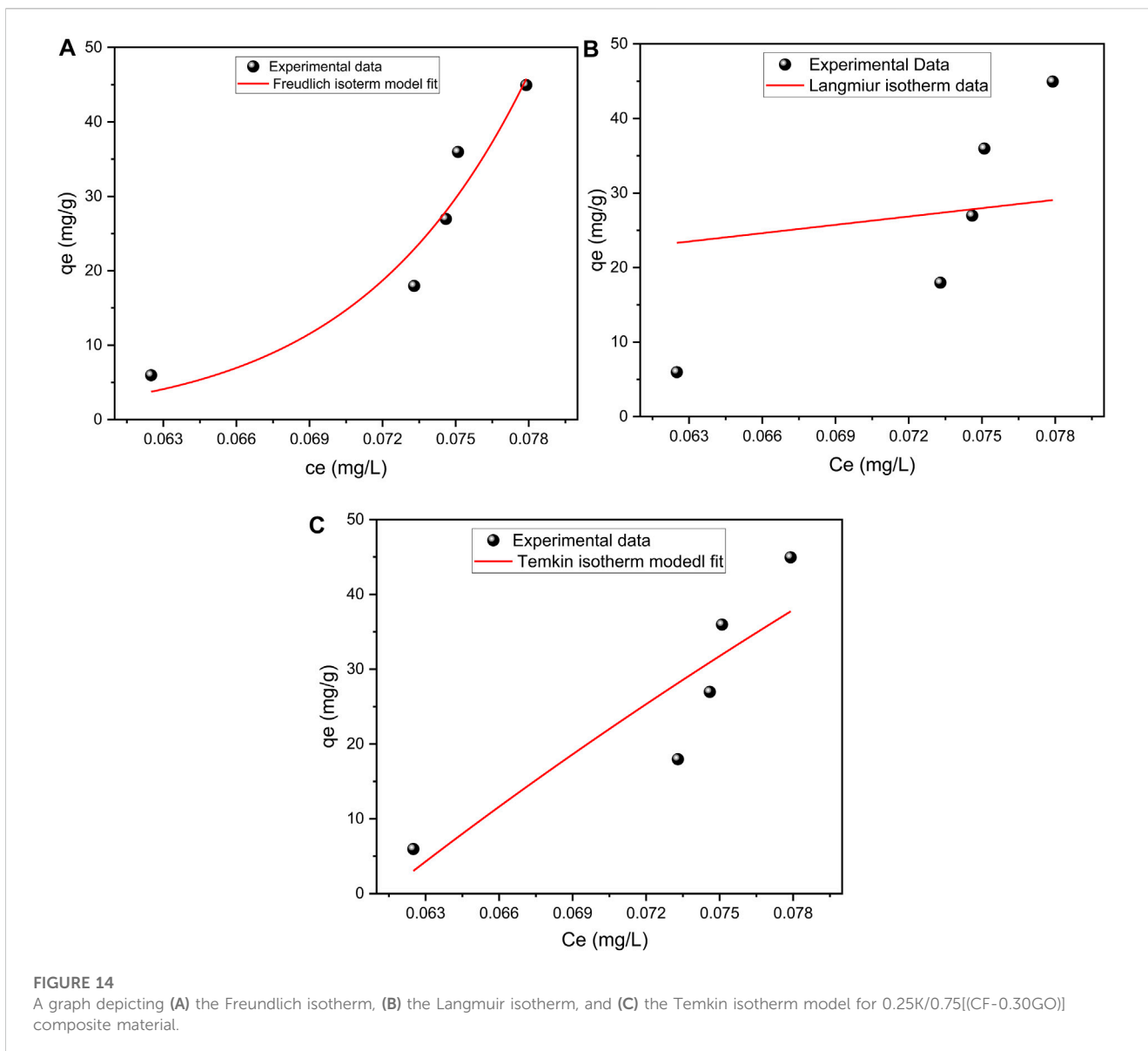


**TABLE 1 Isotherm constants and correlation coefficients by non-linear regression.**

| Isotherm models | Parameters                             | Values          | R <sup>2</sup> |
|-----------------|--|-----------------|----------------|
| Freundlich      | n                                      | 11.37 ± 3.15    | 0.93           |
|                 | K <sub>F</sub> (L g <sup>-1</sup> )    | 1.86E14 ± 1.4   |                |
| Langmuir        | b (1/mg)                               | 0.0036          | 0.24           |
|                 | q <sub>max</sub> (mg g <sup>-1</sup> ) | 104751.37 ± 1.5 |                |
| Temkin          | B <sub>I</sub>                         | 157.52 ± 47     | 0.78           |
|                 | K <sub>T</sub>                         | 16.31 ± 0.9     |                |

appropriate for solid-liquid systems, and the system equation is as follows (Xu et al., 2013; Shukla and Kisku, 2015; Saleh et al., 2016).

For the Pseudo-first-order, the corresponding equation can be written as:

$$\log(q_e - q_t) = \log - \frac{k_1}{2.303}t \tag{7}$$

Where, q<sub>e</sub> and q<sub>t</sub> are the adsorption capacity (mg g<sup>-1</sup>) at equilibrium and time t, respectively, and k<sub>1</sub> is the rate constant of the pseudo-first-order kinetic model. The slope and intercept of the log (q<sub>e</sub>-q<sub>t</sub>) vs. t plot can be used to get the k<sub>1</sub> and q<sub>e</sub> values.

For the Pseudo-second-order, the corresponding equation can be written as:

$$\frac{t}{q_t} = \frac{1}{k_2 q_e^2} + \frac{1}{q_e}t \tag{8}$$

Where q<sub>e</sub> and q<sub>t</sub> are the sorption capability (mg g<sup>-1</sup>) at equilibrium and time t, respectively, and k<sub>2</sub> is that the rate constant of the pseudo-second-order kinetic model. The k<sub>2</sub> and q<sub>e</sub> values may be calculated from the intercept and slope of the plot of t/q<sub>t</sub> against t. Figures 15A, B show the linear

TABLE 2 Parameters for plotting adsorption kinetics for the sample of 0.25K/0.75[(CF-0.30GO)].

| Time (min) | $q_e$ (mg g <sup>-1</sup> ) | $q_t$ (mg g <sup>-1</sup> ) | $q_e - q_t$ | $\text{Log}(q_e - q_t)$ | $t/q_t$ |
|------------|-----------------------------|-----------------------------|-------------|-------------------------|---------|
| 30         | 6.64                        | 6.586                       | 0.054       | -1.267606               | 4.554   |
| 60         | 6.64                        | 6.58                        | 0.06        | -1.221848               | 9.117   |
| 90         | 6.64                        | 6.64                        | 0.0         | -                       | 13.533  |
| 120        | 6.64                        | 6.61                        | 0.03        | -1.522878               | 18.147  |

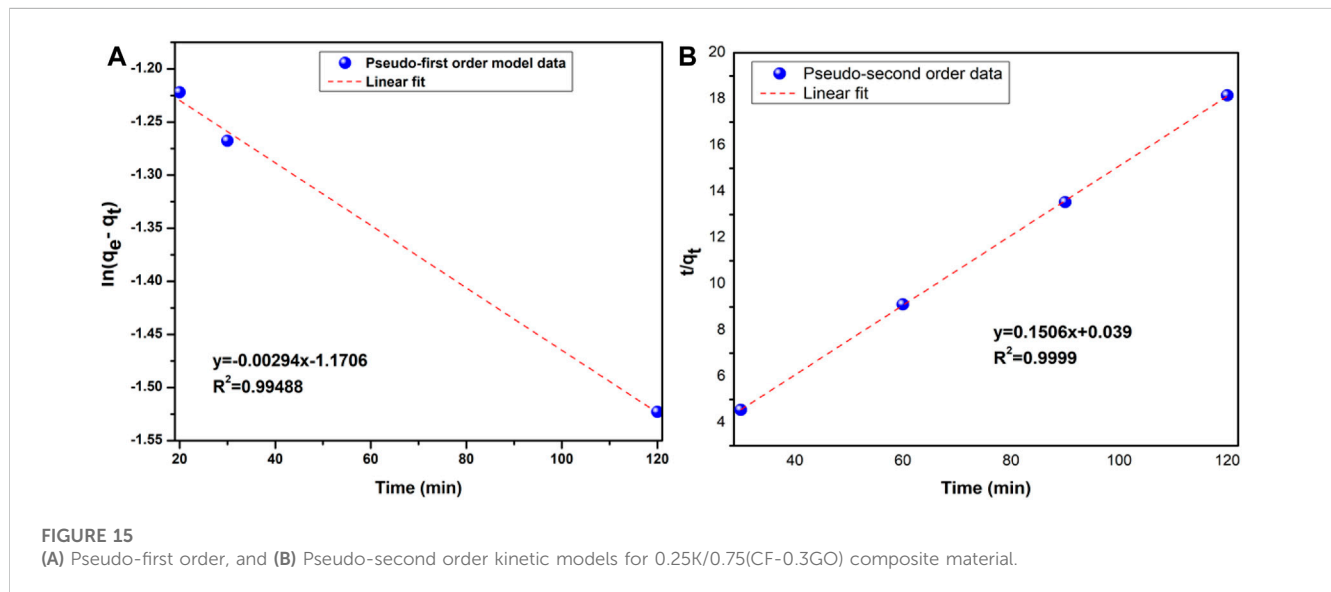


FIGURE 15 (A) Pseudo-first order, and (B) Pseudo-second order kinetic models for 0.25K/0.75(CF-0.30GO) composite material.

TABLE 3 Calculated parameters from Pseudo-first and Pseudo-second-order kinetic models for the sample of 0.25K/0.75[(CF-0.30GO)] composite material.

| Model               | Parameters                                 | Values     | R <sup>2</sup> |
|---------------------|--|------------|----------------|
| Pseudo-first-order  | $q_e, \text{exper.}$ (mg g <sup>-1</sup> ) | 0.06751    | 0.99488        |
|                     | $q_e, \text{calc.}$ (mg g <sup>-1</sup> )  | 6.6405     |                |
|                     | $K_1$ (min <sup>-1</sup> )                 | -0.0000564 |                |
| Pseudo-second-order | $q_e, \text{exper.}$ (mg g <sup>-1</sup> ) | 6.6401     | 0.9999         |
|                     | $q_e, \text{calc.}$ (mg g <sup>-1</sup> )  | 6.6405     |                |
|                     | $K_2$ (min <sup>-1</sup> )                 | 0.5815     |                |

diagrams of the pseudo-first-order and pseudo-second-order kinetic models of Pb (II) adsorption on 0.25K/0.75[(CF-0.30GO)], respectively.

The values of the correlation coefficient ( $R^2$ ) obtained from the linear fitting curve of each model are provided and Table 3 summarizes the fitting parameters. For adsorbent, the  $R^2$  value obtained from the pseudo-first-order model is comparatively low ( $R^2 = 0.99488$ ). In contrast, the pseudo-second-order model is more consistent with the experimental data with  $R^2 = 0.9999$ . Furthermore, the calculated equilibrium adsorption capacity ( $q_{e(\text{cal})}$ ) is very consistent with the experimental equilibrium adsorption capacity ( $q_{e(\text{exp})}$ ).

Based on these results, the pseudo-second-order kinetic model can better describe the adsorption of Pb (II) in 0.25K/0.75[(CF-

0.30GO)]. The pseudo-second-order kinetic model is based on the assumption that the rate-limiting step is controlled by chemical adsorption (Li et al., 2013). This indicates that the adsorption of Pb(II) on 0.25K/0.75[(CF-0.30GO)] composite is controlled by chemical adsorption.

### 3.10 Comparison of specific surface area and adsorption capacity with other adsobers

One of the distinctive qualities of the adsorber that can affect the adsorption process and improve the ability and effectiveness of the adsorption process is the specific surface area and pores in the adsorber surface. Specific surface area values for GCF and K/GCF

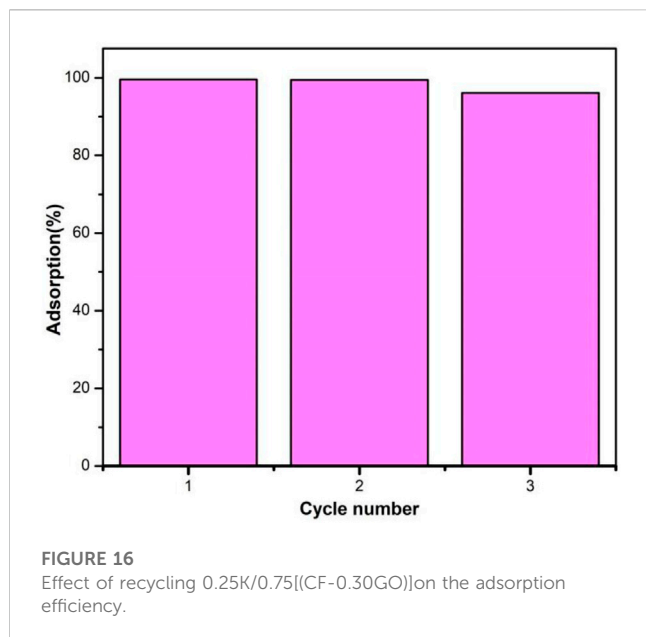


**TABLE 4 Comparison of percentage removal of different adsorbents for lead removal.**

| Adsorbents  | pH | Removal efficiency (%) | References                         |
|---|----|------------------------|------------------------------------|
| GCF   | 2  | 55%                    | This work                          |
| K/GCF   | 2  | 63.5                   | This work                          |
| K/GCF   | 4  | 99                     | This work                          |
| Zeolite-A/reduced GO  | 11 | 93.9                   | Farghali et al. (2021)             |
| natural kaolinite clay  | 6  | 98                     | Jiang et al. (2010)                |
| Melanin-impregnated activated carbon                              | 5  | 91.1                   | Manirethan and Balakrishnan (2020) |
| bentonite modified with imidazole                                 | 5  | 90                     | Kakaei et al. (2020)               |
| CuO/ZnO-tetrapods   | 10 | 97%                    | Sharma et al. (2020)               |
| MnFe <sub>2</sub> O <sub>4</sub> /GO                              | 6  | 98.8                   | Katubi et al. (2021)               |
| ethylenediamine functionalized magnetic GO                        | 4  | 98                     | Zarenezhad et al. (2021)           |
| glutathione-functionalized NiFe <sub>2</sub> O <sub>4</sub> /GO   | 5  | 94                     | Khorshidi et al. (2020)            |
| Polypyrrole-Fe <sub>3</sub> O <sub>4</sub> -seaweed nanocomposite | 5  | 97.2%                  | Sarojini et al. (2021)             |

**TABLE 5 Comparison of the reuse capacities of different adsorbents for lead removal.**

| Adsorbent   | No. of cycles | Removal efficiency (%) | References                  |
|---|---------------|------------------------|-----------------------------|
| K/GCF   | 3             | 96.2                   | This work                   |
| Polypyrrole-Fe <sub>3</sub> O <sub>4</sub> -seaweed nanocomposite | 2             | 94.5                   | Sarojini et al. (2021)      |
|   | 5             | 62.5                   |                             |
| Nanochitosan/sodium alginate/microcrystalline cellulose beads     | 2             | 93                     | Vijayalakshmi et al. (2017) |
| Magnetic inverse Fe <sub>3</sub> O <sub>4</sub> nanoparticles     | 5             | 80                     | Lingamdinne et al. (2017)   |

were 266.20 m<sup>2</sup>/g and 577.11 m<sup>2</sup>/g, respectively, according to the lead ion adsorption method. The capacity and efficiency of adsorbents are determined by a variety of elements, including the adsorbent's primary source, techniques of modification, and active sites present on the adsorbent surface. At pH 4, the removal efficiency of the optimized ternary composite (K/GCF) was 99% in this study. Furthermore, at pH 2, the optimized binary composite (GCF) and K/GCF removal efficiencies were 55% and 63.5%, demonstrating that uniform particle dispersion improves the surface area and performance of the ternary composite sample. The lead removal efficiency of GCF and K/GCF was compared with the results of other adsorbents at different pH values (Table 4). The results reveal that the generated adsorbents are more feasible for adsorbing the lead ion from aqueous solutions than many other adsorbents.

### 3.11 Reusability of the adsorbent

The 0.25K/0.75[(CF-0.30GO)] adsorbent was tested for up to three adsorption-desorption cycles for the reuse of Pb (II) aqueous solution (Figure 16). The test was done at the optimized pH value (at pH of 4) and reaction time (90 min) at room temperature. The results show that as the adsorption-desorption stage increases, the adsorption percentage of Pb (II) decreases. This decrease in efficiency may be related to the damage or change of the active center of the adsorbent (Foroutan et al., 2020b). The removal efficiency of the lead ion using the present adsorbent was 99.5, 99.4, and 96.2% in the first, second, and third cycles, respectively. In addition, it should be noted that at the third cycle of the adsorption process, the reduction in the amount of Pb (II) adsorption using the adsorbent is less than 4%. The results show that the obtained adsorbent can be used for up to three cycles to remove lead ions from an aqueous solution without significantly reducing the adsorption capacity. Table 5 compares the reusability of the produced nanocomposite with that of different sorbents. The repeated adsorption/desorption process decreases the contaminant level to a lower volume.

## 4 Conclusion

In this study, Graphene oxide, CoFe<sub>2</sub>O<sub>4</sub>, CoFe<sub>2</sub>O<sub>4</sub>-GO (CF-GO), and K/(CF-GO) were successfully synthesized by improved, hydrothermal, and solution methods, respectively. Among the binary composites, CF-0.3GO showed a better adsorption capacity of about 23.6 mg g<sup>-1</sup> from the binary composite samples at the initial Pb concentration of 50 mg L<sup>-1</sup>. In

addition, the sample with a composition of 0.25K/0.75[(CF-0.30GO)] showed the best adsorption capacity of about  $4.2 \text{ mg g}^{-1}$  at the initial Pb concentration of  $10 \text{ mg L}^{-1}$  from the ternary composites and was selected for further studies. The materials were characterized using XRD, SEM, FTIR, and TGA-DTA. The XRD results showed that the pretreated clay was contained a high content of kaolinite clay with little quartz amount. The XRD pattern of the synthesized  $\text{CoFe}_2\text{O}_4$  and GO confirmed the formation of pure  $\text{CoFe}_2\text{O}_4$  particles and graphene oxide. The effective formation of the ternary composite was also confirmed by the XRD results. The FTIR data of (CF-GO)/K confirmed the presence of various oxygen-containing functional groups which enhance the adsorption capacity by the reactions of Pb (II) with active surface groups. TGA-DTA data revealed that the thermal stability of kaolinite enhanced with the incorporation of  $\text{CoFe}_2\text{O}_4$  and GO through the structure. The effect of pH (2–10) and contact time (30–90 min) were also studied for 0.25K/0.75 [(CF-0.30GO)] composite. At pH of 4, the adsorption capacity and removal efficiency was  $6.62 \text{ mg g}^{-1}$  and 99 %, respectively, and becomes constant. Adsorption studies revealed that the adsorption capacity of ternary composites can be well described by the Freundlich isotherm model. The adsorption kinetics best fitted with Pseudo-second-order adsorption. Finally, the reusability of the present composite was studied after separating the catalyst magnetically for up to 3 cycles with a small reduction in removal efficiency. Therefore, the experimental results of this study specify that the present composite could be a potential candidate for the removal of Pb (II).

## Data availability statement

The original contributions presented in the study are included in the article/[Supplementary Material](#), further inquiries can be directed to the corresponding authors.

## Author contributions

YD: Conceptualization, Data curation, Formal Analysis, Investigation, Methodology, Resources, Software, Visualization, Writing–original draft, Writing–review and editing. TD: Conceptualization, Data curation, Formal Analysis, Funding acquisition, Investigation, Methodology, Project administration,

Resources, Software, Supervision, Validation, Visualization, Writing–review and editing.

## Funding

The authors declare financial support was received for the research, authorship, and/or publication of this article. This research project was funded by Adama Science and Technology University under the number ASTU/SM-R/216/21, Adama, Ethiopia.

## Acknowledgments

We would like to express our gratitude to Material Science and Engineering department, Adama Science and Technology University, Ethiopia for their technical competence and financial support in carrying out this study.

## Conflict of interest

The authors declare that the research was conducted in the absence of any commercial or financial relationships that could be construed as a potential conflict of interest.

## Publisher's note

All claims expressed in this article are solely those of the authors and do not necessarily represent those of their affiliated organizations, or those of the publisher, the editors and the reviewers. Any product that may be evaluated in this article, or claim that may be made by its manufacturer, is not guaranteed or endorsed by the publisher.

## Supplementary material

The Supplementary Material for this article can be found online at: <https://www.frontiersin.org/articles/10.3389/fmats.2023.1277467/full#supplementary-material>

## References

- Ahmed, M. A., Ahmed, M. A., and Mohamed, A. A. (2022). Facile adsorptive removal of dyes and heavy metals from wastewaters using magnetic nanocomposite of zinc ferrite@ reduced graphene oxide. *Inorg. Chem. Commun.* 144, 109912. doi:10.1016/j.inoche.2022.109912
- Alatalo, S.-M., Repo, E., Mäkilä, E., Salonen, J., Vakkilainen, E., and Sillanpää, M. (2013). Adsorption behavior of hydrothermally treated municipal sludge & pulp and paper industry sludge. *Bioresour. Technol.* 147, 71–76. doi:10.1016/j.biortech.2013.08.034
- Alshameri, A., He, H., Xin, C., Zhu, J., Xinghu, W., Zhu, R., et al. (2019). Understanding the role of natural clay minerals as effective adsorbents and alternative source of rare earth elements: adsorption operative parameters. *Hydrometallurgy* 185, 149–161. doi:10.1016/j.hydromet.2019.02.016
- Asadi, R., Abdollahi, H., Gharabaghi, M., and Boroumand, Z. (2020). Effective removal of Zn (II) ions from aqueous solution by the magnetic  $\text{MnFe}_2\text{O}_4$  and  $\text{CoFe}_2\text{O}_4$  spinel ferrite nanoparticles with focuses on synthesis, characterization, adsorption, and desorption. *Adv. Powder Technol.* 31 (4), 1480–1489. doi:10.1016/j.apt.2020.01.028
- Bany-Aiesh, H., Banat, R., and Al-Sou'od, K. (2015). Kinetics and adsorption isotherm of ibuprofen onto grafted  $\beta$ -beta;-CD/Chitosan polymer. *Am. J. Appl. Sci.* 12 (12), 917–930. doi:10.3844/ajassp.2015.917.930
- Beatrice, O. O., and Olusola, O. O. (2020). A review on the application of clay minerals as heavy metal adsorbents for remediation purposes. *Environ. Technol. Innovation* 18, 100692. doi:10.1016/j.eti.2020.100692
- Boix, G., Troyano, J., Garzón-Tovar, L., Camur, C., Bermejo, N., Yazdi, A., et al. (2020). MOF-beads containing inorganic nanoparticles for the simultaneous removal of multiple heavy metals from water. *ACS Appl. Mater. Interfaces* 12 (9), 10554–10562. doi:10.1021/acsami.9b23206
- Chai, J.-B., Au, P. I., Mubarak, N. M., Khalid, M., Ng, W. P. Q., Jagadish, P., et al. (2020). Adsorption of heavy metal from industrial wastewater onto low-cost Malaysian kaolin clay-based adsorbent. *Environ. Sci. Pollut. Res.* 27 (12), 13949–13962. doi:10.1007/s11356-020-07755-y
- Chen, P., Li, H., Song, S., Weng, X., He, D., and Zhao, Y. (2017). Adsorption of dodecylamine hydrochloride on graphene oxide in water. *Results Phys.* 7, 2281–2288. doi:10.1016/j.rinp.2017.06.054
- Chen, Q., Yin, D., Zhu, S., and Hu, X. (2012). Adsorption of cadmium (II) on humic acid coated titanium dioxide. *J. Colloid Interface Sci.* 367 (1), 241–248. doi:10.1016/j.jcis.2011.10.005

- Darder, M., Colilla, M., and Ruiz-Hitzky, E. (2005). Chitosan–clay nanocomposites: application as electrochemical sensors. *Appl. Clay Sci.* 28 (1–4), 199–208. doi:10.1016/j.clay.2004.02.009
- Das, S., Samanta, A., Gangopadhyay, G., and Jana, S. (2018). Clay-based nanocomposites as recyclable adsorbent toward Hg (II) capture: experimental and theoretical understanding. *ACS omega* 3 (6), 6283–6292. doi:10.1021/acsomega.8b00789
- Deliyanni, E., Kyzas, G. Z., Triantafyllidis, K. S., and Matis, K. A. (2015). Activated carbons for the removal of heavy metal ions: a systematic review of recent literature focused on lead and arsenic ions. *Open Chem.* 13. doi:10.1515/chem-2015-0087
- Elass, K., Laachach, A., Alaoui, A., and Azzi, M. (2011). Removal of methyl violet from aqueous solution using a stevensite-rich clay from Morocco. *Appl. Clay Sci.* 54 (1), 90–96. doi:10.1016/j.clay.2011.07.019
- Es-sabhany, H., Berradi, M., Nkhili, S., Hsissou, R., Allaoui, M., Loutfi, M., et al. (2019). Removal of heavy metals (nickel) contained in wastewater-models by the adsorption technique on natural clay. *Mater. Today Proc.* 13, 866–875. doi:10.1016/j.matpr.2019.04.050
- Fang, H., Meng, F., Yan, J., Chen, G. y., Zhang, L., Wu, S., et al. (2019). Fe 3 O 4 hard templating to assemble highly wrinkled graphene sheets into hierarchical porous film for compact capacitive energy storage. *RSC Adv.* 9 (35), 20107–20112. doi:10.1039/c9ra02132a
- Farghali, M. A., Abo-Aly, M. M., and Salaheldin, T. A. (2021). Modified mesoporous zeolite-A/reduced graphene oxide nanocomposite for dual removal of methylene blue and Pb<sup>2+</sup> ions from wastewater. *Inorg. Chem. Commun.* 126, 108487. doi:10.1016/j.inoche.2021.108487
- Findk, S. (2023). Conventional and sono-assisted adsorption of methyl violet using synthesized magnetic kaolin supported copper ferrite and zinc ferrite. *Arabian J. Sci. Eng.*, 1–14. doi:10.1007/s13369-023-08213-w
- Fiyadh, S. S., AlSaadi, M. A., Jaafar, W. Z., AlOmar, M. K., Fayaed, S. S., Mohd, N. S., et al. (2019). Review on heavy metal adsorption processes by carbon nanotubes. *J. Clean. Prod.* 230, 783–793. doi:10.1016/j.jclepro.2019.05.154
- Foroutan, R., Mohammadi, R., MousaKhanloo, F., Sahebi, S., Ramavandi, B., Kumar, P. S., et al. (2020a). Performance of montmorillonite/graphene oxide/CoFe<sub>2</sub>O<sub>4</sub> as a magnetic and recyclable nanocomposite for cleaning methyl violet dye-laden wastewater. *Adv. Powder Technol.* 31 (9), 3993–4004. doi:10.1016/j.apt.2020.08.001
- Foroutan, R., Mohammadi, R., Peighambaroust, S. J., Jalali, S., and Ramavandi, B. (2020b). Application of nano-silica particles generated from offshore white sandstone for cadmium ions elimination from aqueous media. *Environ. Technol. Innovation* 19, 101031. doi:10.1016/j.eti.2020.101031
- Foroutan, R., Mohammadi, R., Razeghi, J., and Ramavandi, B. (2019). Performance of algal activated carbon/Fe<sub>3</sub>O<sub>4</sub> magnetic composite for cationic dyes removal from aqueous solutions. *Algal Res.* 40, 101509. doi:10.1016/j.algal.2019.101509
- Fu, Y., and Wang, X. (2011). Magnetically separable ZnFe<sub>2</sub>O<sub>4</sub>–graphene catalyst and its high photocatalytic performance under visible light irradiation. *Industrial Eng. Chem. Res.* 50 (12), 7210–7218. doi:10.1021/ie200162a
- Ghiloufi, I., Ghouli, J. E., Modwi, A., and Mir, L. E. (2016). Ga-doped ZnO for adsorption of heavy metals from aqueous solution. *Mater. Sci. Semicond. Process.* 42, 102–106. doi:10.1016/j.mssp.2015.08.047
- Giraldo, L., Erto, A., and Moreno-Piraján, J. C. (2013). Magnetite nanoparticles for removal of heavy metals from aqueous solutions: synthesis and characterization. *Adsorption* 19 (2), 465–474. doi:10.1007/s10450-012-9468-1
- Hayati, B., Maleki, A., Najafi, F., Gharibi, F., McKay, G., Gupta, V. K., et al. (2018). Heavy metal adsorption using PAMAM/CNT nanocomposite from aqueous solution in batch and continuous fixed bed systems. *Chem. Eng. J.* 346, 258–270. doi:10.1016/j.cej.2018.03.172
- He, K., Chen, G., Zeng, G., Chen, A., Huang, Z., Shi, J., et al. (2018). Enhanced removal performance for methylene blue by kaolin with graphene oxide modification. *J. Taiwan Inst. Chem. Eng.* 89, 77–85. doi:10.1016/j.jtice.2018.04.013
- Huang, X., Tian, J., Li, Y., Yin, X., and Wu, W. (2020). Preparation of a three-dimensional porous graphene oxide–kaolinite–poly (vinyl alcohol) composite for efficient adsorption and removal of ciprofloxacin. *Langmuir* 36 (37), 10895–10904. doi:10.1021/acs.langmuir.0c00654
- Ji, Z., Shen, X., Zhu, G., Zhou, H., and Yuan, A. (2012). Reduced graphene oxide/nickel nanocomposites: facile synthesis, magnetic and catalytic properties. *J. Mater. Chem.* 22 (8), 3471–3477. doi:10.1039/c2jm14680k
- Jiang, M.-q., Jin, X. y., Lu, X. Q., and Chen, Z. I. (2010). Adsorption of Pb (II), Cd (II), Ni (II) and Cu (II) onto natural kaolinite clay. *Desalination* 252 (1–3), 33–39. doi:10.1016/j.desal.2009.11.005
- Kakaei, S., Khameneh, E. S., Rezazadeh, F., and Hosseini, M. H. (2020). Heavy metal removing by modified bentonite and study of catalytic activity. *J. Mol. Struct.* 1199, 126989. doi:10.1016/j.molstruc.2019.126989
- Katubi, K. M. M., Alsaiani, N. S., Alzahrani, F. M., M. Siddeeq, S., and A. Tahooun, M. (2021). Synthesis of manganese ferrite/graphene oxide magnetic nanocomposite for pollutants removal from water. *Processes* 9 (4), 589. doi:10.3390/pr9040589
- Khorshidi, P., Shirazi, R. H. S. M., Miralinaghi, M., Moniri, E., and Saadi, S. (2020). Adsorptive removal of mercury (II), copper (II), and lead (II) ions from aqueous solutions using glutathione-functionalized NiFe 2 O 4/graphene oxide composite. *Res. Chem. Intermed.* 46, 3607–3627. doi:10.1007/s11164-020-04164-1
- Kikuchi, Y., Qian, Q., Machida, M., and Tatsumoto, H. (2006). Effect of ZnO loading to activated carbon on Pb (II) adsorption from aqueous solution. *Carbon* 44 (2), 195–202. doi:10.1016/j.carbon.2005.07.040
- Koby, M., Demirbas, E., Senturk, E., and Ince, M. (2005). Adsorption of heavy metal ions from aqueous solutions by activated carbon prepared from apricot stone. *Bioresour. Technol.* 96 (13), 1518–1521. doi:10.1016/j.biortech.2004.12.005
- Lee, G. F. (1975). “Role of hydrous metal oxides in the transport of heavy metals in the environment,” in *Heavy metals in the aquatic environment* (Oxford: Pergamon), 137–147.
- Lee, L. Z., Zaini, M. A. A., and Tang, S. H. (2019). “Porous nanomaterials for heavy metal removal,” in *Handbook of ecomaterials*. Editors L. M. T. Martínez, O. V. Kharisova, and B. I. Kharisov (Cham: Springer International Publishing), 469–494.
- Lertcumfu, N., Jaita, P., Thammarong, S., Lamkhao, S., Tandorn, S., Randorn, C., et al. (2020). Influence of graphene oxide additive on physical, microstructure, adsorption, and photocatalytic properties of calcined kaolinite-based geopolymer ceramic composites. *Colloids And Surfaces A Physicochem. And Eng. Aspects* 602, 125080. doi:10.1016/j.colsurfa.2020.125080
- Li, H., Huang, G., An, C., Hu, J., and Yang, S. (2013). Removal of tannin from aqueous solution by adsorption onto treated coal fly ash: kinetic, equilibrium, and thermodynamic studies. *Industrial Eng. Chem. Res.* 52 (45), 15923–15931. doi:10.1021/ie402054w
- Li, J., Feng, H., Jiang, J., Feng, Y., Xu, Z., and Qian, D. (2015). One-pot *in situ* synthesis of a CoFe 2 O 4 nanoparticle-reduced graphene oxide nanocomposite with high performance for levodopa sensing. *RSC Adv.* 5 (121), 99669–99677. doi:10.1039/c5ra15379d
- Lindholm, J. (2004). “Development and validation of HPLC methods for analytical and preparative purposes,” in *Acta universitatis upsaliensis*.
- Lingamdinne, L. P., Chang, Y. Y., Yang, J. K., Singh, J., Choi, E. H., Shiratani, M., et al. (2017). Biogenic reductive preparation of magnetic inverse spinel iron oxide nanoparticles for the adsorption removal of heavy metals. *Chem. Eng. J.* 307, 74–84. doi:10.1016/j.cej.2016.08.067
- Liu, X.-M., Fu, S.-Y., and Zhu, L.-P. (2007). High-yield synthesis and characterization of monodisperse sub-microsized CoFe<sub>2</sub>O<sub>4</sub> octahedra. *J. Solid State Chem.* 180 (2), 461–466. doi:10.1016/j.jssc.2006.11.003
- Lo, S.-F., Wang, S. Y., Tsai, M. J., and Lin, L. D. (2012). Adsorption capacity and removal efficiency of heavy metal ions by Moso and Ma bamboo activated carbons. *Chem. Eng. Res. Des.* 90 (9), 1397–1406. doi:10.1016/j.cherd.2011.11.020
- Manirethan, V., and Balakrishnan, R. M. (2020). Batch and continuous studies on the removal of heavy metals using biosynthesised melanin impregnated activated carbon. *Environ. Technol. Innovation* 20, 101085. doi:10.1016/j.eti.2020.101085
- Marcano, D. C., Kosynkin, D. V., Berlin, J. M., Sinititskii, A., Sun, Z., Slesarev, A., et al. (2010). Improved synthesis of graphene oxide. *ACS nano* 4 (8), 4806–4814. doi:10.1021/nn1006368
- Mathew, D. S., and Juang, R.-S. (2007). An overview of the structure and magnetism of spinel ferrite nanoparticles and their synthesis in microemulsions. *Chem. Eng. J.* 129 (1–3), 51–65. doi:10.1016/j.cej.2006.11.001
- Melikoglu, A. Y., Bilek, S. E., and Cesur, S. (2019). Optimum alkaline treatment parameters for the extraction of cellulose and production of cellulose nanocrystals from apple pomace. *Carbohydr. Polym.* 215, 330–337. doi:10.1016/j.carbpol.2019.03.103
- Mnasri-Ghnimi, S., and Frini-Srasra, N. (2019). Removal of heavy metals from aqueous solutions by adsorption using single and mixed pillared clays. *Appl. Clay Sci.* 179, 105151. doi:10.1016/j.clay.2019.105151
- Monear, N. C., and Xhabija, B. (2020). The effect of lead during the Flint water crisis on mouse embryonic stem cells self-renewal and differentiation markers. *Toxicol. Vitro* 63, 104719. doi:10.1016/j.tiv.2019.104719
- Mustapha, S., Ndamitso, M., Abdulkareem, A., Tijani, J., Mohammed, A., and Shuaib, D. (2019). Potential of using kaolin as a natural adsorbent for the removal of pollutants from tannery wastewater. *Heliyon* 5 (11), e02923. doi:10.1016/j.heliyon.2019.e02923
- Naem, H., Ajmal, M., Qureshi, R. B., Muntha, S. T., Farooq, M., and Siddiq, M. (2019). Facile synthesis of graphene oxide–silver nanocomposite for decontamination of water from multiple pollutants by adsorption, catalysis and antibacterial activity. *J. Environ. Manag.* 230, 199–211. doi:10.1016/j.jenvman.2018.09.061
- Nejadshafiee, V., and Islami, M. R. (2019). Adsorption capacity of heavy metal ions using sulfone-modified magnetic activated carbon as a bio-adsorbent. *Mater. Sci. Eng. C* 101, 42–52. doi:10.1016/j.msec.2019.03.081
- Obasi, P. N., and Akudinobi, B. B. (2020). Potential health risk and levels of heavy metals in water resources of lead–zinc mining communities of Abakaliki, southeast Nigeria. *Appl. Water Sci.* 10 (7), 184. doi:10.1007/s13201-020-01233-z
- Obayomi, K. S., and Auta, M. (2019). Development of microporous activated Al<sub>2</sub>O<sub>3</sub> clay for adsorption of lead (II) ions from aqueous solution. *Heliyon* 5 (11), e02799. doi:10.1016/j.heliyon.2019.e02799

- Olusegun, S. J., and Mohallem, N. D. (2020). Comparative adsorption mechanism of doxycycline and Congo red using synthesized kaolinite supported CoFe<sub>2</sub>O<sub>4</sub> nanoparticles. *Environ. Pollut.* 260, 114019. doi:10.1016/j.envpol.2020.114019
- Ray, P. Z., and Shipley, H. J. (2015). Inorganic nano-adsorbents for the removal of heavy metals and arsenic: a review. *RSC Adv.* 5 (38), 29885–29907. doi:10.1039/c5ra02714d
- Ren, H., Li, H., Fan, H., Qi, G., and Liu, Y. (2023). Facile synthesis of CoFe<sub>2</sub>O<sub>4</sub>-graphene oxide nanocomposite by high-gravity reactor for removal of Pb (II). *Sep. Purif. Technol.* 305, 122472. doi:10.1016/j.seppur.2022.122472
- Romero-Guerrero, L., Moreno-Tovar, R., Arenas-Flores, A., Marmolejo Santillán, Y., and Pérez-Moreno, F. (2018). Chemical, mineralogical, and refractory characterization of kaolin in the regions of huayacocotla-alumbres, Mexico. *Adv. Mater. Sci. Eng.* 2018, 1–11. doi:10.1155/2018/8156812
- Saleh, T. A., Sari, A., and Tuzen, M. (2016). Chitosan-modified vermiculite for as (III) adsorption from aqueous solution: equilibrium, thermodynamic and kinetic studies. *J. Mol. Liq.* 219, 937–945. doi:10.1016/j.molliq.2016.03.060
- Santhosh, C., Kollu, P., Felix, S., Velmurugan, V., Jeong, S. K., and Grace, A. N. (2015). CoFe<sub>2</sub>O<sub>4</sub> and NiFe<sub>2</sub>O<sub>4</sub>@graphene adsorbents for heavy metal ions – kinetic and thermodynamic analysis. *RSC Adv.* 5 (37), 28965–28972. doi:10.1039/c5ra02905h
- Sarojini, G., Venkateshbabu, S., and Rajasimman, M. (2021). Facile synthesis and characterization of polypyrrole-iron oxide-seaweed (PPy-Fe<sub>3</sub>O<sub>4</sub>-SW) nanocomposite and its exploration for adsorptive removal of Pb (II) from heavy metal bearing water. *Chemosphere* 278, 130400. doi:10.1016/j.chemosphere.2021.130400
- Sharma, M., Poddar, M., Gupta, Y., Nigam, S., Avasthi, D., Adelung, R., et al. (2020). Solar light assisted degradation of dyes and adsorption of heavy metal ions from water by CuO-ZnO tetrapodal hybrid nanocomposite. *Mater. Today Chem.* 17, 100336. doi:10.1016/j.mtchem.2020.100336
- Shukla, S., and Kisku, G. (2015). Linear and non-linear kinetic modeling for adsorption of disperse dye in batch process. *Res. J. Environ. Toxicol.* 9 (6), 320–331. doi:10.3923/rjet.2015.320.331
- Sumathi, S., and Kirankumar, V. S. (2016). *Catalytic and electrical study of substituted cobalt ferrite.*
- Tan, P., Sun, J., Hu, Y., Fang, Z., Bi, Q., Chen, Y., et al. (2015). Adsorption of Cu<sup>2+</sup>, Cd<sup>2+</sup> and Ni<sup>2+</sup> from aqueous single metal solutions on graphene oxide membranes. *J. Hazard. Mater.* 297, 251–260. doi:10.1016/j.jhazmat.2015.04.068
- Temkin, M., and Pyzhev, V. (1940). *Recent modifications to Langmuir isotherms.*
- Triantafyllidou, S., and Lambrinidou, Y. (2009). Lead (Pb) exposure through drinking water: lessons to be learned from recent U.S. experience. *Glob. Nest J.* 11.
- Tul Aïn, Q., Haq, S. H., Alshammari, A., Al-Mutlaq, M. A., and Anjum, M. N. (2019). The systemic effect of PEG-nGO-induced oxidative stress *in vivo* in a rodent model. *Beilstein J. Nanotechnol.* 10, 901–911. doi:10.3762/bjnano.10.91
- Veeramachineni, A. K., Sathasivam, T., Muniyandy, S., Janarthanan, P., Langford, S., and Yan, L. (2016). Optimizing extraction of cellulose and synthesizing pharmaceutical grade carboxymethyl sago cellulose from Malaysian sago pulp. *Appl. Sci.* 6 (6), 170. doi:10.3390/app6060170
- Verma, B., and Balomajumder, C. (2020). Surface modification of one-dimensional Carbon Nanotubes: a review for the management of heavy metals in wastewater. *Environ. Technol. Innovation* 17, 100596. doi:10.1016/j.eti.2019.100596
- Vijayalakshmi, K., Devi, B. M., Latha, S., Gomathi, T., Sudha, P., Venkatesan, J., et al. (2017). Batch adsorption and desorption studies on the removal of lead (II) from aqueous solution using nanochitosan/sodium alginate/microcrystalline cellulose beads. *Int. J. Biol. Macromol.* 104, 1483–1494. doi:10.1016/j.ijbiomac.2017.04.120
- Wang, D., Zhang, G., Zhou, L., Wang, M., Cai, D., and Wu, Z. (2017). Synthesis of a multifunctional graphene oxide-based magnetic nanocomposite for efficient removal of Cr (VI). *Langmuir* 33 (28), 7007–7014. doi:10.1021/acs.langmuir.7b01293
- Wang, W., Guo, S., Zhang, D., and Yang, Z. (2019). One-pot hydrothermal synthesis of reduced graphene oxide/zinc ferrite nanohybrids and its catalytic activity on the thermal decomposition of ammonium perchlorate. *J. Saudi Chem. Soc.* 23 (2), 133–140. doi:10.1016/j.jscs.2018.05.001
- Wu, L., Ye, Y., Liu, F., Tan, C., Liu, H., Wang, S., et al. (2013). Organo-bentonite-Fe<sub>3</sub>O<sub>4</sub> poly(sodium acrylate) magnetic superabsorbent nanocomposite: synthesis, characterization, and Thorium(IV) adsorption. *Appl. Clay Sci.* 83–84, 405–414. doi:10.1016/j.clay.2013.07.012
- Xu, H., Chen, Y., Huang, H., Liu, Y., and Yang, Z. (2013). Removal of lead (II) and cadmium (II) from aqueous solutions using spent *Agaricus bisporus*. *Can. J. Chem. Eng.* 91 (3), 421–431. doi:10.1002/cjce.21671
- Yadav, D. K., and Srivastava, S. (2017). Carbon nanotubes as adsorbent to remove heavy metal ion (Mn<sup>2+</sup>) in wastewater treatment. *Mater. Today Proc.* 4 (2), 4089–4094. Part A. doi:10.1016/j.matpr.2017.02.312
- Yadav, V. B., Gadi, R., and Kalra, S. (2019a). Clay based nanocomposites for removal of heavy metals from water: a review. *J. Environ. Manage* 232, 803–817. doi:10.1016/j.jenvman.2018.11.120
- Yadav, V. B., Gadi, R., and Kalra, S. (2019b). Clay based nanocomposites for removal of heavy metals from water: a review. *J. Environ. Manage* 232, 803–817. doi:10.1016/j.jenvman.2018.11.120
- Yan, L., Li, S., Yu, H., Shan, R., Du, B., and Liu, T. (2016). Facile solvothermal synthesis of Fe<sub>3</sub>O<sub>4</sub>/bentonite for efficient removal of heavy metals from aqueous solution. *Powder Technol.* 301, 632–640. doi:10.1016/j.powtec.2016.06.051
- Yao, L., Hou, X., Hu, S., Wang, J., Li, M., Su, C., et al. (2014). Green synthesis of mesoporous ZnFe<sub>2</sub>O<sub>4</sub>/C composite microspheres as superior anode materials for lithium-ion batteries. *J. Power Sources* 258, 305–313. doi:10.1016/j.jpowsour.2014.02.055
- Yari, M., Rajabi, M., Moradi, O., Yari, A., Asif, M., Agarwal, S., et al. (2015). Kinetics of the adsorption of Pb (II) ions from aqueous solutions by graphene oxide and thiol functionalized graphene oxide. *J. Mol. Liq.* 209, 50–57. doi:10.1016/j.molliq.2015.05.022
- Zarenezhad, M., Zarei, M., Ebratkhanan, M., and Hosseinzadeh, M. (2021). Synthesis and study of functionalized magnetic graphene oxide for Pb<sup>2+</sup> removal from wastewater. *Environ. Technol. Innovation* 22, 101384. doi:10.1016/j.eti.2021.101384
- Zawrah, M. (2018). *Characterization of sol-gel fabricated cobalt ferrite CoFe<sub>2</sub>O<sub>4</sub> nanoparticles.*
- Zen, S., El Berrichi, F., Abidi, N., Duplay, J., Jada, A., and Gasmı, B. (2018). Activated kaolin's potential adsorbents for the removal of Derma Blue R67 acid dye: kinetic and thermodynamic studies. *Desalination Water Treat.* 112, 196–206. doi:10.5004/dwt.2018.21996
- Zhang, Y., Yan, L., Xu, W., Guo, X., Cui, L., Gao, L., et al. (2014). Adsorption of Pb (II) and Hg (II) from aqueous solution using magnetic CoFe<sub>2</sub>O<sub>4</sub>-reduced graphene oxide. *J. Mol. Liq.* 191, 177–182. doi:10.1016/j.molliq.2013.12.015
- Zhao, G., Ren, X., Gao, X., Tan, X., Li, J., Chen, C., et al. (2011). Removal of Pb (II) ions from aqueous solutions on few-layered graphene oxide nanosheets. *Dalton Trans.* 40 (41), 10945–10952. doi:10.1039/c1dt11005e
- Zheng, Y., Cheng, B., Fan, J., Yu, J., and Ho, W. (2021). Review on nickel-based adsorption materials for Congo red. *J. Hazard. Mater.* 403, 123559. doi:10.1016/j.jhazmat.2020.123559
- Zong, M., Huang, Y., Wu, H., Zhao, Y., Wang, Q., and Sun, X. (2014). One-pot hydrothermal synthesis of RGO/CoFe<sub>2</sub>O<sub>4</sub> composite and its excellent microwave absorption properties. *Mater. Lett.* 114, 52–55. doi:10.1016/j.matlet.2013.09.113